From Strong to Weak Correlations in Breathing-Mode Kagome van der Waals Materials $Nb_3(F, Cl, Br, I)_8$ as a Robust and Versatile Platform for Many-Body Engineering

Aretz, Joost; Grytsiuk, Sergii; Liu, Xiaojing; Feraco, Giovanna; Knekna, Chrystalla; Waseem, Muhammad; Dan, Zhiying; Bianchi, Marco; Ali, Mazhar N.; More Authors

DOI
10.1103/wr7w-nfhg

Licence
CC BY

Publication date
2025

Document Version
Final published version

Published in
Physical Review X

Citation (APA)
Aretz, J., Grytsiuk, S., Liu, X., Feraco, G., Knekna, C., Waseem, M., Dan, Z., Bianchi, M., Ali, M. N., & More Authors (2025). From Strong to Weak Correlations in Breathing-Mode Kagome van der Waals Materials: $Nb_3(F, Cl, Br, I)_8$ as a Robust and Versatile Platform for Many-Body Engineering. *Physical Review X*, *15*(4), Article 041042. https://doi.org/10.1103/wr7w-nfhg

From Strong to Weak Correlations in Breathing-Mode Kagome van der Waals Materials: $\mathrm{Nb_3(F,Cl,Br,I)_8}$ as a Robust and Versatile Platform for Many-Body Engineering

Joost Aretz,[1] Sergii Grytsiuk,[1] Xiaojing Liu,[2] Giovanna Feraco,[2] Chrystalla Knekna,[2,3] Muhammad Waseem,[2]
Zhiying Dan,[2] Marco Bianchi,[4] Philip Hofmann,[4] Mazhar N. Ali,[5] Mikhail I. Katsnelson,[1,6]
Antonija Grubišić-Čabo,[2] Hugo U. R. Strand,[7] Erik G. C. P. van Loon,[8] and Malte Rösner[1,9,*]

[1]*Institute for Molecules and Materials, Radboud University,*
Heijendaalseweg 135, 6525AJ Nijmegen, The Netherlands
[2]*Zernike Institute for Advanced Materials, University of Groningen, 9747 AG Groningen, The Netherlands*
[3]*Van der Waals-Zeeman Institute, Institute of Physics, University of Amsterdam,*
Science Park 904, 1098 XH, Amsterdam, The Netherlands
[4]*Department of Physics and Astronomy, Interdisciplinary Nanoscience Center (iNANO),*
Aarhus University, 8000 Aarhus C, Denmark
[5]*Kavli Institute of Nanoscience, Delft University of Technology,*
Lorentzweg 1, 2628 CJ Delft, the Netherlands
[6]*Constructor Knowledge Institute, Constructor University, Campus Ring 1, 28759 Bremen, Germany*
[7]*School of Science and Technology, Örebro University, SE-701 82 Örebro, Sweden*
[8]*NanoLund and Division of Mathematical Physics, Department of Physics, Lund University, Lund, Sweden*
[9]*Faculty of Physics, Bielefeld University, 33501 Bielefeld, Germany*

(Received 17 February 2025; revised 21 July 2025; accepted 3 November 2025; published 5 December 2025)

By combining *ab initio* downfolding with cluster dynamical mean-field theory, we study the degree of correlations in monolayer, bilayer, and bulk breathing-mode kagome van der Waals materials $\mathrm{Nb_3(F,Cl,Br,I)_8}$. Our new material-specific many-body model library shows that in low-temperature bulk structures the Coulomb correlation strength steadily increases from I to Br, Cl, and F, allowing us to identify $\mathrm{Nb_3I_8}$ as a weakly correlated insulator whose gap is only mildly affected by the local Coulomb interaction. $\mathrm{Nb_3Br_8}$ and $\mathrm{Nb_3Cl_8}$ are strongly correlated insulators, whose gaps are significantly influenced by Coulomb-induced vertex corrections. $\mathrm{Nb_3F_8}$ is a prototypical bulk Mott insulator whose gap is initially opened by strong correlation effects. Angle-resolved photoemission spectroscopy measurements comparing $\mathrm{Nb_3Br_8}$ and $\mathrm{Nb_3I_8}$ allow us to experimentally confirm these findings by revealing spectroscopic footprints of the degree of correlation. Our calculations further uncover how the thickness and the stacking affect the degree of correlations and predict that the entire material family can be tuned into correlated charge transfer or Mott-insulating phases upon electron or hole doping. Our magnetic property analysis based on our model parameter library additionally confirms that interlayer magnetic interactions likely drive the lattice phase transition to the low-temperature structures. The accompanying bilayer hybridization through interlayer dimerization yields magnetic singlet-like ground states in the Cl, Br, and I compounds. We further prove that all low-temperature compounds are dynamically stable and that electron-phonon coupling to the low-energy subspace is suppressed. Our findings establish $\mathrm{Nb_3X_8}$ as a robust, versatile, and tunable class for van der Waals-based Coulomb and Mott engineering with a rich phase diagram and allow us to speculate on the symmetry-breaking effects necessary for the recently observed Josephson diode effect in $\mathrm{NbSe_2/Nb_3Br_8/NbSe_2}$ heterostructures.

DOI: 10.1103/wr7w-nfhg

Subject Areas: Condensed Matter Physics,
Strongly Correlated Materials

I. INTRODUCTION

Correlation effects resulting from electron-electron (Coulomb) interactions are omnipresent in solids. Depending on the relative Coulomb interaction strength, they manifest in various ways, starting from renormalizations of quasiparticle dispersions in the case of weak correlations [1], via induced shake-off or replica bands in the case of intermediate correlations [2,3], or in form of

---

[*] Contact author: malte.roesner@uni-bielefeld.de

completely different ground states in the case of strong correlations [4,5]. Being able to tune the degree of correlations would therefore allow us to engineer many-body properties of quantum materials [6].

The layered structure of van der Waals (vdW) materials makes them uniquely tunable [7], with opportunities such as field-effect-doping [8,9], substrate engineering [10], heterostructuring [7], and moiré engineering [11], but also via chemical modifications [6]. Furthermore, within the library of layered vdW materials, we now have access to a variety of correlated ground states including magnetism [12], charge-density wave (CDW) order [13], superconductivity [14,15], as well as Mott insulators [11,16,17]. However, the complex electronic structure of the systems in question and the inherent complexity and partial fragility of correlated electron physics make it challenging to fully understand the microscopic origin of the observed phenomena, let alone making predictive simulations. Thus, simple and robust correlated layered material systems with varying and tunable degrees of correlation strengths are highly desirable.

Here, we show that the transition metal halide family Nb_3X_8 holds up to this promise. These so-called breathing-mode kagome vdW materials [18] host only one band per monolayer close to the Fermi level, which is cleanly separated from the rest of the electronic structure as a result of in-plane trimerization of the transition metal atoms. In multilayer structures this further competes with an out-of-plane dimerization, especially at low temperatures.

Using *ab initio* downfolding to molecular orbitals, we derive material-specific minimal models, including single-particle (hopping) and many-body screened Coulomb interaction matrix elements for the entire family Nb_3X_8, with $X \in \{F, Cl, Br, I\}$ across monolayer, bilayer, and bulk structures. Studying them using cluster dynamical mean-field theory [19] shows how the balance between kinetic and screened Coulomb interaction energies changes from Nb_3F_8 to Nb_3I_8 as well as from monolayer to bulk structures. In this way, we prove that Nb_3X_8 realizes several correlated phases ranging from weakly correlated band insulators to correlated insulators and strongly correlated Mott insulators, which we summarize in the generalized phase diagram spanned by the in-plane versus out-of-plane correlation strengths, as shown in Fig. 1. We further clarify the distinction between the band insulator and correlated insulator through experimental angle-resolved photoemission spectroscopy and by theoretically investigating their response to charge doping. Finally, we present a fully *ab initio* investigation of the magnetic ground state properties of all low-temperature bulk compounds and specifically on the high- to low-temperature phase transition in Nb_3Cl_8 and Nb_3Br_8. This finally allows us to suggest a new mechanism for time-reversal symmetry-breaking in finite stacks of Nb_3X_8, which is needed to understand the experimentally observed Josephson diode effect in $NbSe_2/Nb_3Br_8/NbSe_2$ heterostructures.

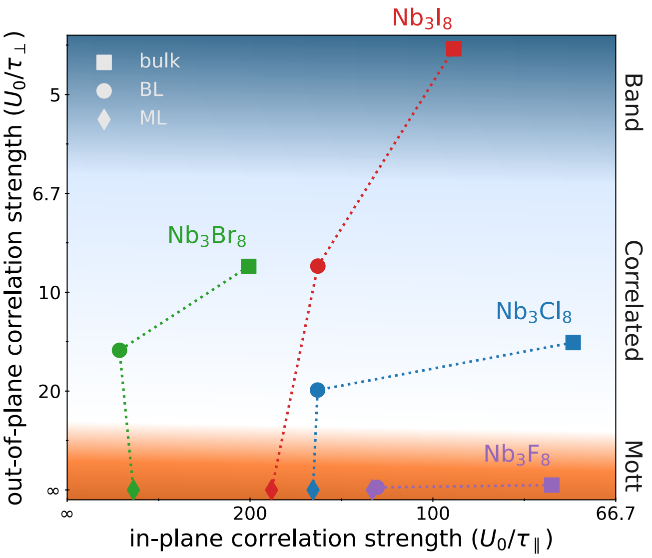

FIG. 1. Phase diagram of Nb_3X_8 for monolayer, bilayer, and bulk structures in the low-temperature ($R\bar{3}m$) phase. The horizontal axis measures the in-plane correlation strength and the vertical axis the out-of-plane correlation strength with $\tau_\parallel$, $\tau_\perp$ and U_0 being material and structure specific effective in- and out-of-plane hopping and local Coulomb interaction matrix elements. The phase space is divided into Mott, correlated, and band insulators.

A. Nb_3X_8 overview

Nb_3X_8 belongs to the class of layered vdW kagome materials, which are intensively studied due to the interplay of their non-trivial electronic band topology and intriguing electron correlation phenomena [18,20]. Nb_3X_8 specifically belongs to the subclass of breathing-mode kagome materials, with alternating in-plane bond lengths, as illustrated in Fig. 2. Among them, Nb_3Cl_8 and Nb_3Br_8 have recently gained much attention due to their promises to represent prototypical single-band or few-band Mott insulators [21–26], possibly accompanied by strongly correlated magnetic ground states [21,24,27–29]. Nb_3Br_8 has received further attention due to its role in inducing field-free Josephson diode effects in $NbSe_2/Nb_3Br_8/NbSe_2$ heterostructures [30]. Although some scenarios have been suggested [31], it is not yet clear what microscopic behavior yields the required symmetry breakings and whether it is intrinsic to Nb_3Br_8 or related to the interfaces.

Experimentally, x-ray diffraction shows lattice phase transitions in Nb_3Cl_8 and Nb_3Br_8 from high- to low-temperature structures, which can be understood as a shift in the vdW layer stacking [32,33]. Raman spectroscopy [34] corroborates this interpretation but also indicates that phonon symmetries are not affected by the transition. Angle-resolved photoemission spectroscopy (ARPES) data show gapped electronic structures with rather flat, albeit broadened, bands below the Fermi level for bulk Nb_3I_8 [35], Nb_3Cl_8 [36], and Nb_3Br_8 [25,37], as well as their admixtures [23].

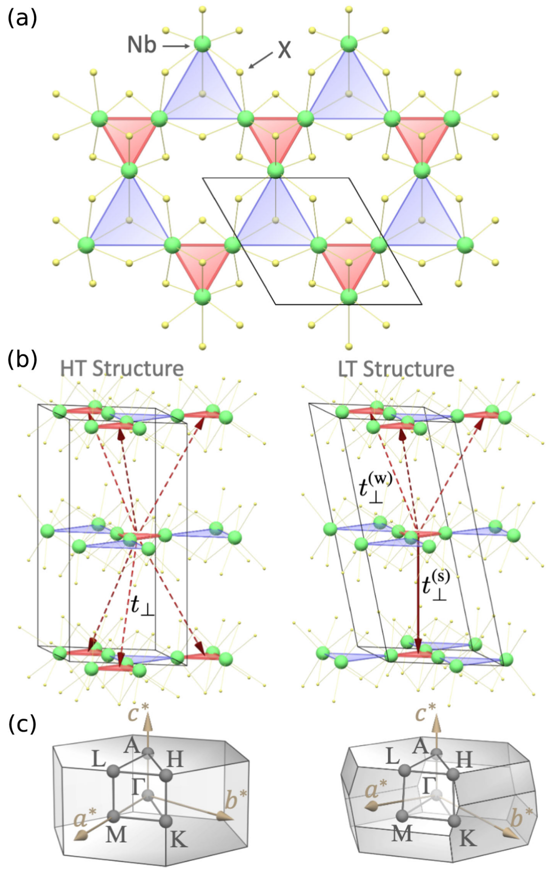

FIG. 2. Nb_3X_8 crystal structures. (a) Single layer (top view) and (b) bulk structures (side view) in the LT ($R\bar{3}m$) and HT ($P\bar{3}m1$) phase. Darker red solid (dashed) arrows indicate strong (weak) interlayer couplings $t_\perp^s$ ($t_\perp^w$) between the nearest trimers. The gray lines in (a) and (b) represent the primitive unit cell. (c) The Brillouin zones and high-symmetry points for both structures.

Spectral gaps in Nb_3Cl_8 have also been reported from transport measurements [26,38]. For $Nb_3Cl_{8-x}Br_x$, magnetic susceptibilities further show Curie-Weiss behavior at elevated temperatures in the high-temperature phases, accompanied by sudden drops upon entering the low-temperature phases [23,27,29,32,33,36,39]. This has been interpreted as a transition from a paramagnetic to a nonmagnetic phase, and the finite susceptibility at very low temperatures is ascribed to magnetic impurities [32,33].

Theoretically, the modeling of these materials takes place in several steps. A first impression is given by density functional theory (DFT), which has been used to study the monolayer, bilayer, and bulk structures, in both low- and high-temperature crystal structures [22,24,35,40,41]. Starting with the monolayer, DFT shows a single, rather flat band crossing the Fermi level, which is half filled and thus hosts exactly one electron per unit cell. At low temperatures and going to bilayer and bulk structures, there is an alternating strong and weak hybridization between adjacent layers, which leads to a dimerization in the out-of-plane direction [22–25,29]. In this case, DFT predicts two rather flat bands around the Fermi level, which show a small, but finite hybridization gap. Since flat bands are indicators for low kinetic energies, the role of competing Coulomb interactions needs to be carefully taken into account. Mean-field DFT calculations are, however, known to underestimate the impact of the latter, especially in the case of *d* orbitals which dominate the low-energy space in the case of Nb_3X_8. Therefore, beyond mean-field theories, which take possibly strong Coulomb interactions accurately into account, are necessary. So far this has been done only inconsistently for monolayer Nb_3Cl_8 [21,23,29,42], generic bilayer models approximating Nb_3Cl_8 and Nb_3Br_8 [22], as well as for simplified models of bulk Nb_3Cl_8 [24] and Nb_3Br_8 [25] using different variants of higher-level many-body theory or alternative supercell approaches [43]. All of these calculations hint towards an intriguing interplay between enhanced Coulomb interactions and kinetic energies, which seem to drive variants of Mott insulating states. For bulk structures, this especially requires a careful analysis of the impact of the out-of-plane dimerization, which has so far only been discussed qualitatively for bilayers of Nb_3Br_8 and Nb_3Cl_8 [22] as well as for bulk Nb_3Br_8 [25]. Most importantly, the role of screening and its impact to the actual material-specific Coulomb interactions along the Nb_3X_8 family members has not been studied yet.

II. RESULTS

To systematically, material specifically, and quantitatively study these effects, we calculate and investigate all kinetic and Coulomb interaction terms of Nb_3X_8 with $X \in \{F, Cl, Br, I\}$ in their monolayer, bilayer, and bulk forms and solve the resulting models using cluster dynamical mean-field theory. Since the high-temperature structure of Nb_3I_8 has not been observed yet and since correlation effects are most intriguing in the low-temperature phases, we mostly focus on the latter in the following and will only comment on differences in the high-temperature structures of Nb_3Cl_8 and Nb_3Br_8 where appropriate. We further put a special focus on the Coulomb interactions and, most importantly, their screening to uncover the exact microscopic origin of various resulting phases. We apply the same formalism to all studied compounds allowing for direct comparisons.

A. Nb_3X_8 crystal structure

The breathing-mode kagome structure depicted in Fig. 2(a) yields an in-plane trimerization of Nb atoms (see small triangles in red). In the out-of-plane direction, there exist two stackings, referred to as the high- (HT) and low-temperature (LT) structures, which are depicted in Fig. 2(b) together with their Brillouin zones in Fig. 2(c). The LT stacking leads to a dimerization in the out-of-plane direction with alternating strong and weak hybridization between adjacent layers, as indicated by dashed and solid line arrows in Fig. 2(b) and discussed in more detail below. Nb_3Cl_8 and Nb_3Br_8 undergo a structural phase transition that changes the stacking from the HT to the LT structures at around 90 and 380K, respectively [29,32,33,39,44]. While it is hypothesized that Nb_3I_8 exhibits a similar transition at even higher temperatures, this has yet to be confirmed experimentally.

At high temperatures, crystals of both Nb_3Cl_8 and Nb_3Br_8 belong to the $P\bar{3}m1$ space group. However, at low temperatures, Nb_3Br_8 and Nb_3I_8 have been reported to adopt the $R\bar{3}m$ space group [39,44]. In contrast, the LT crystal structure of Nb_3Cl_8 has been described inconsistently in different studies, with reported space groups of $R3$ [33], $R\bar{3}m$ [34,39,44], and $C2/m$ [32]. For consistency we adopt in the following the $R\bar{3}m$ point group for Nb_3Cl_8 and note that a symmetry reduction has minimal impact on the correlation effects and electronic structure [24,29]. To the best of our knowledge, only Nb_3Cl_8, Nb_3Br_8, and Nb_3I_8 have been synthesized, but the addition of $Nb_3F_8^*$ gives a unified view of the full series. To emphasize that $Nb_3F_8^*$ is putative, we will use the starred notation.

To get a homogeneous crystal structure set, we perform for all compounds in their LT bulk phases (and for Nb_3Cl_8 and Nb_3Br_8 also in their HT phases) a lattice and structural optimization keeping only the space group fixed to $R\bar{3}m$ ($P\bar{3}m1$). We find all of them, including the putative $Nb_3F_8^*$, to be dynamically stable as further discussed in Sec. V B. The mono- and bilayer structures are taken from these relaxed bulk phases by introducing an appropriate vacuum spacing.

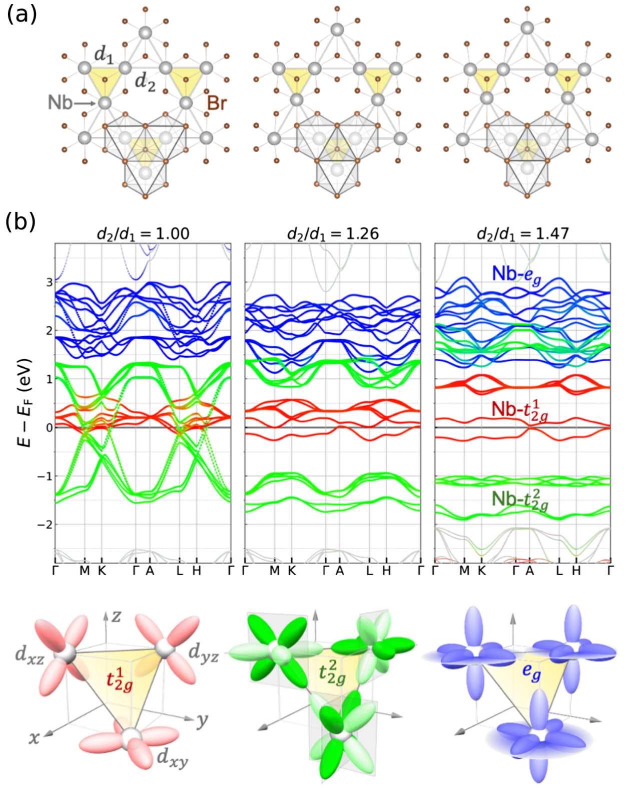

FIG. 3. Breathing mode induced flat band formation in LT ($R\bar{3}m$) Nb_3Br_8. (a) and (b) The crystal structure (showing only one layer for clarity) and the electronic structure as a function of the size ratio of the small and large triangles d_2/d_1. The electronic structures in (b) are weighted between $Nb - t_{2g}^1$ (in red), $Nb - t_{2g}^2$ (in green), and Nb-e_g (in blue) states, respectively. Black lines in (a) depict the ideal (left panel) and distorted (two following panels) octahedral environment surrounding the Nb atoms.

B. Electronic structure

1. In-plane trimerization as the origin of robust flat bands

The formation of flat bands in Nb_3X_8 plays a crucial role in their electronic and magnetic properties. As the underlying lattice structure is of kagome type, it has been suspected that the flat bands originate from the topologically nontrivial flat bands of the well-known generic kagome band structure as described, e.g., by tight-binding models with isotropic hoppings; see, for example, Refs. [36,45]. However, as the low energetic orbitals of all Nb_3X_8 compounds are of predominant Nb d character, this simplified picture has to be reconsidered [46]. Therefore, we calculated the electronic structure of LT Nb_3Br_8 at different levels of the breathing mode perturbation and thus degree of in-plane Nb trimerization, which is measured by the ratio d_2/d_1, where d_1 and d_2 represent the sizes of the small and large triangles, respectively, cf. Fig. 3(a). When the structure is a conventional kagome lattice ($d_1 = d_2$), the octahedral crystal field causes the d orbitals of the Nb ions to split into the lower-energy t_{2g} (d_{xy}, d_{yz}, and d_{xz}) and the higher-energy e_g ($d_{x^2-y^2}$ and d_{z^2}) states. In the actual breathing-mode ground state ($d_2/d_1 \approx 1.47$), the octahedral crystal field is distorted, and the t_{2g} states are further split into two sublevels labeled t_{2g}^1 and t_{2g}^2.

In Fig. 3(b) we show the corresponding DFT band structures, starting from the unperturbed conventional kagome lattice ($d_2/d_1 = 1$) and indicate Nb t_{2g}^1 orbitals in red, Nb t_{2g}^2 orbitals in green, and Nb e_g orbitals in blue. From this, we see that in the putative conventional kagome structure, Nb_3Br_8 would be a metal with various Nb d bands crossing the Fermi level. Upon trimerization, i.e., upon introducing the breathing mode perturbation, we see that the Nb t_{2g}^2 bands open up a full gap, while the Nb t_{2g}^1 bands stay behind, nearly pinned to the Fermi level. Finally, in the actual full breathing mode structure ($d_2/d_1 \approx 1.47$), we see that the Nb t_{2g}^1 bands further split into a set of two very flat bands located directly around the Fermi level and a set of four unoccupied bands. Next to this, we also find that the occupied Nb t_{2g}^2 bands split, yielding two sets of very flat bands, while their unoccupied counterparts only mildly change in their dispersion and now overlap in energy with the Nb e_g bands.

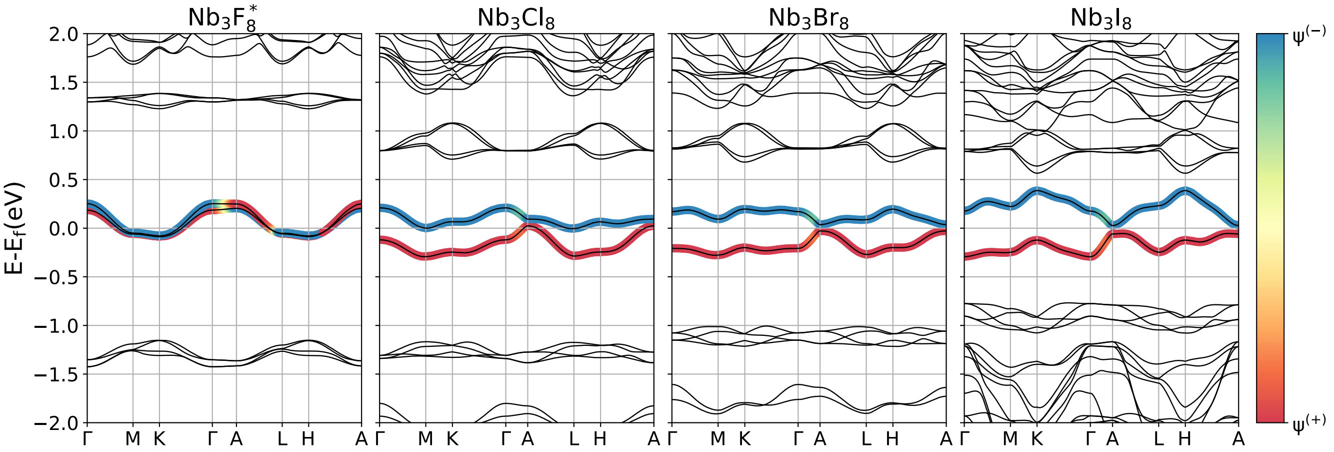

FIG. 4. LT ($R\bar{3}m$) Nb_3X_8 DFT band structures. Colors indicate the weight of the bonding ($\psi^{(+)}$) and antibonding ($\psi^{(-)}$) orbitals in the Wannier basis. $\psi^{(\pm)} = |\langle\psi^{(\pm)}|\psi\rangle|^2$, where $|\psi\rangle$ is the eigenfunction in the Wannier basis.

The flat band formation in Nb_3X_8 is thus intimately connected to the Nb trimerization within the breathing mode distortion and independent of the LT or HT stacking. In the monolayer limit, we already showed that the Nb t_{1g} band at the Fermi level can be best understood as being formed by a molecular orbital centered at the breathing-mode induced Nb trimer [24]. As such, the origin of the two well-separated low-energy flat bands around the Fermi level in Nb_3X_8 is conceptually very similar to the formation of flat bands in the star-of-David phase of TaS_2 [13] or twisted bilayer graphene [47]: due to new, larger structures (induced by the CDW in TaS_2, the moiré potential in twisted bilayer graphene, or here the breathing-mode distortion), new effective orbitals are formed, which are spatially rather far apart from each other. This large spatial separation yields a small effective hopping of electrons between these new effective CDW, moiré, or here molecular orbitals, such that their resulting bands are only weakly dispersive. Simultaneously, gaps in the rest of the electronic structures are opened, leaving (nearly) isolated flat bands behind. All of this is lifted upon destroying the larger structure, i.e., by melting the CDW in TaS_2, tuning away from the magic angle in twisted bilayer graphene, or suppressing the breathing mode distortion in Nb_3X_8.

The key advantage of Nb_3X_8 is that its breathing mode distortion is a stable ground state (at all reported temperatures and doping levels) that does not require a precisely tuned twist angle or temperature-induced stabilization. The formation of flat bands in Nb_3X_8 is thus very robust, so that resulting correlation effects can be studied without additional complications.

2. Out-of-plane dimerization as origin of flat band gapping

Having established the in-plane breathing mode distortion and its accompanying trimerization as the mechanism producing the isolated flat bands, we are now ready to study their evolution throughout the Nb_3X_8 family. In Fig. 4, we show the bulk DFT band structures in the LT phases. As expected, we find two relatively flat bands around the Fermi level in all cases. In the case of $Nb_3F_8^*$, both bands cross the Fermi level, while for the others, we consistently find one fully occupied and one completely unoccupied band. For in-plane momenta ($k_z = 0$), the two bands are clearly split apart, while for the out-of-plane momentum direction $\Gamma - A$, we observe a stronger dispersion, and the gap nearly closes. As will become clear from the subsequent Wannierization discussed below, this k_z behavior is a result of the interlayer dimerization of trimers within the strongly hybridized bilayers in the LT structure. Thus, in k_z, the low-energetic electronic structure is reminiscent of the behavior of the Su-Schrieffer-Heeger (SSH) model [48], which consequently yields a gap in this direction, due to the mismatch of the alternating out-of-plane hopping matrix elements in the LT phase. From Cl to Br and I, we already see the first clear trend in the material class: the in-plane gap between these two bands steadily increases. In the HT phase, this out-of-plane dimerization is strongly suppressed yielding negligible gaps, rendering the low-energy band structures of all HT structures qualitatively similar to the LT $Nb_3F_8^*$ one.

3. Molecular orbital basis

To prepare for the derivation of material-specific many-body Hamiltonians using *ab initio* downfolding and to further analyze the low-energetic band structure, we construct maximally localized Wannier functions for the two low-energy bands. In all four cases, we find that the bands can be perfectly Wannier interpolated within a basis spanned by two molecular orbitals ψ_1 and ψ_2, which are centered on trimers of adjacent layers and which are directly above each other, see Fig. 5. As shown in Refs. [21,24], these molecular orbitals arise from a direct linear combination of three Nb d orbitals from the local trimers. The original atomistic

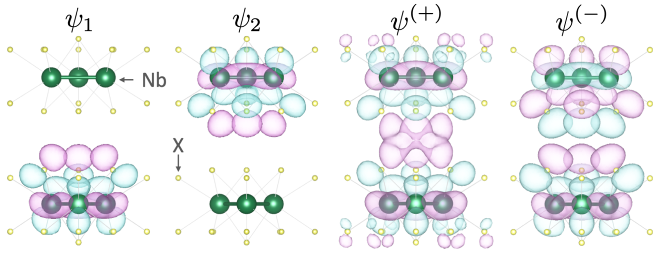

FIG. 5. Wannier molecular orbitals of LT ($R\bar{3}m$) Nb_3Br_8. ψ_1 and ψ_2, along with their bonding ($+$) and antibonding ($-$) combinations, $\psi^{(\pm)} = (\psi_1 \pm \psi_2)/\sqrt{2}$.

multiorbital basis has, however, very little influence due to the large energy separation between the trimer orbital and all other states, which are therefore either fully occupied or empty. In this molecular orbital basis, we find similar contributions of both orbitals to both low-energy bands. However, upon diagonalization of the single-particle Wannier Hamiltonian, we find that the lower (occupied) band is well described by a bonding orbital $\psi^{(+)}$ formed by the direct sum of the trimer-centered molecular orbitals $\psi^{(+)} = (\psi_1 + \psi_2)/\sqrt{2}$, while the upper (unoccupied) band is well described by the corresponding antibonding orbital $\psi^{(-)} = (\psi_1 - \psi_2)/\sqrt{2}$, as illustrated in Fig. 5. For the subsequent analysis of correlation effects this molecular orbital basis is most efficient, as it compresses six atomistic basis orbitals to just two molecular ones. Furthermore, it will be helpful to switch back and forth between the molecular orbital basis (ψ_i) and the bonding-antibonding basis ($\psi^{(\pm)}$), as the self-energy in the LT phase becomes diagonal in the bonding-antibonding basis.

Upon projecting the Kohn-Sham states to the $\psi^{(\pm)}$ basis, we see that this interpretation holds especially for in-plane momenta. For out-of-plane k_z momenta, however, we observe that $\psi^{(\pm)}$ states mix, which is a result of the small, but finite wave function overlap between the dimerized layers. This admixture thus verifies the SSH-like behavior in the k_z direction and is consistent with Ref. [49] within which Nb_3Br_8 and Nb_3I_8 are classified as obstructed atomic insulators [50]. The latter are characterized by wave function centers that are not located at an atomic position, which holds in our case for the bonding combination of the trimer orbitals, cf. $\psi^{(+)}$ in Fig. 5. Although the Cl, Br, and I compounds all share the classification as obstructed atomic insulators, the details and specifically the size of the DFT gap change from material to material, as reflected in the Wannier hopping parameters in Table I and as discussed in more detail in the following section.

C. Downfolded many-body Hamiltonians from *ab initio* constrained random phase approximation calculations

Using the molecular orbital basis, we proceed with deriving generalized Hubbard Hamiltonians of the form

$$H = \sum_{i,j} t_{ij} c_i^\dagger c_j + \frac{1}{2} \sum_{i,j,k,l} U_{ijkl} c_i^\dagger c_j^\dagger c_k c_l \qquad (1)$$

for all compounds. Here $c_i^\dagger$ and c_j are electron creation and annihilation operators in molecular orbitals at sites i and j, respectively, t_{ij} are single-particle (hopping) and U_{ijkl} partially screened two-particle (Coulomb) matrix elements. The latter are evaluated within the constrained random

TABLE I. Structural and *ab initio* downfolded many-body Hamiltonian parameters for LT ($R\bar{3}m$) Nb_3X_8. In-plane (a) and out-of-plane (c) lattice parameters, molecular orbital spread (Ω), nearest neighbor in-plane ($t_\parallel$), and out-of-plane ($t_\perp^{(s/w)}$) hopping parameters corresponding to hoppings illustrated in Fig. 2(b) and corresponding cRPA screened Coulomb ($U_\parallel$ and $U_\perp$) interactions, on-site bare (V_0) and screened (U_0) Coulomb interactions including their ratio $\varepsilon_{\mathrm{eff}} = V_0/U_0$. t, U, and V are provided in meV. Note that this Table only shows the most relevant model parameters. Hubbard-I and cluster DMFT calculations were performed with all calculated hopping parameters and the full Coulomb tensor U_{ijkl} on and between dimerized molecular orbitals.

X		a (Å)	c (Å)	Ω (Å^2)	$t_\parallel$	$t_\perp^{(s)}$	$t_\perp^{(w)}$	V_0	U_0	$\varepsilon_{\mathrm{eff}}$	$U_\parallel$	$U_\perp^{(s)}$	$U_\perp^{(w)}$
F	Bulk	5.74	31.16	4.12	34.3	−4.9	−6.5	7486.4	2590.5	2.89	804.5	714.6	572.5
	BL				33.8	−5.0		7496.2	3988.8	1.88	1977.2	1987.7	
	ML				33.6			7497.2	4021.8	1.86	2016.7		
Cl	Bulk	6.75	36.75	7.08	20.1	−136.0	−16.1	6126.4	1451.4	4.22	475.6	400.1	313.5
	BL				18.5	−136.2		6150.0	2697.6	2.28	1598.5	1570.9	
	ML				18.6			6180.3	2771.3	2.23	1670.1		
Br	Bulk	7.08	40.84	8.54	5.9	−169.4	−20.4	5787.4	1186.6	4.88	381.5	342.0	262.4
	BL				3.4	−169.2		5819.4	2396.0	2.43	1483.8	1482.3	
	ML				4.5			5887.7	2475.3	2.38	1554.3		
I	Bulk	7.70	43.24	13.15	−8.3	−218.2	−24.6	5052.7	787.0	6.42	258.3	258.5	183.8
	BL				−13.2	−218.4		5101.7	1928.7	2.65	1323.3	1349.0	
	ML				−11.5			5321.1	2052.4	2.59	1397.3		

phase approximation (cRPA) [51], which accounts for all RPA-level screening processes except those taking place within the molecular orbitals ψ_i. In this way, all intra- and interlayer screening properties are included in the model, without any double-counting occurring when the model is solved. As a first-principles method, the cRPA therefore captures how screening differs across the class of materials, both due to changes in the chemical composition as well as due to differences in the screening environment between monolayers, bilayers, and bulk structures. This way, our material-specific localized molecular orbitals render adequately the different local chemical environments in each compound and in each stacking, while the screening captures global crystal effects including polarizations from higher and deeper lying electronic states.

The cRPA scheme gives access to the full tensor U_{ijkl}. In Table I, we show a subset of these matrix elements focusing on the local and nearest-neighbor density-density Coulomb (U_{ijji}) as well as on intra- and interlayer hopping matrix elements. For a complete overview and details about the calculations, see Sec. V A.

We start by discussing the molecular orbital spreads (Ω) of the bulk structures, which we find to increase from F to I. This trend follows the lattice constants, which increase in the in- and out-of-plane direction from F to I. This shows how the molecular orbitals and thus the local orbital basis reflects the chemical changes in the structure. The tightest-bound lattice ($Nb_3F_8^*$) hosts highly localized molecular orbitals, while the weakest-bound lattice (Nb_3I_8) has rather delocalized molecular orbitals.

These trends are further reflected in the hopping matrix elements. Overall, we find that the in-plane nearest-neighbor hopping ($t_\parallel$) shows a decreasing trend from F to I. Its magnitude is relatively small in all compounds, which reflects the flat in-plane (constant k_z) dispersion. The strong out-of-plane nearest-neighbor hopping ($t_\perp^{(s)}$), in turn, grows significantly in magnitude from F to I, which is in line with a increase in the orbital spread. The "weak link" in the out-of-plane directions ($t_\perp^{(w)}$) is in all compounds about an order of magnitude smaller than $t_\perp^{(s)}$ and increases in magnitude slightly from F to I. This reflects the increasing bilayer hybridization between the interlayer dimerized trimers, leading to the growth of the bonding-antibonding splitting, as observed around Γ in Fig. 4. In $Nb_3F_8^*$, the in- and out-of-plane hoppings are not very different, such that there is no opening of a full dimerization gap throughout the Brillouin zone and only a small splitting at Γ is observed. To analyze the gap at the high symmetry point A, we need to take into account that there are three adjacent layer neighbors in the weak-link directions, such that the SSH gap of a nearest-neighbor model would be given by $\tau_\perp = 2|t_\perp^{(s)} - \sqrt{3}t_\perp^{(w)}|$. This increases from about 216 to 351 meV going from Cl to I, indicating an increase of the dimerization strength (in $Nb_3F_8^*$, it is only 4 meV). The DFT gaps at A (where the SSH gap opens) are, however of similar size in Nb_3Cl_8 and Nb_3Br_8. We understand this as a result of long-range hoppings suppressing the dimerization, particularly hopping to next nearest and next-next-nearest neighboring trimers in the adjacent van der Waals layer. These hoppings become slightly more pronounced from Cl to I.

The most important interaction parameter is the partially screened local density-density interaction U_0 (Hubbard's U), which depends on the size of the orbital and on the screening. We can disentangle these effects by also looking at the bare local density-density Coulomb interaction V_0, which depends only on the size of the orbital. It is largest in $Nb_3F_8^*$ and smallest in Nb_3I_8, inversely following the molecular orbital spread. The impact of screening can then be quantified by the ratio $\varepsilon_{\text{eff}} = V_0/U_0$, which is seen to increase drastically from F to I. This screening parameter is approximately inversely proportional to the "background" electronic gap (i.e., the gap between the filled and occupied bands above and below the flat bands). Thus, the screened local density-density Coulomb interactions are not just suppressed by the enhanced molecular orbital spread, but also by stronger screening going from F to I.

Next to this, our calculations show that the partially screened Coulomb interactions are dominated by density-density interactions. This is a result of having just a single molecular orbital being centered in each of the adjacent, strongly hybridized monolayers. Non-density-density interactions, such as Hund's exchange interactions, are thus nonlocal, which significantly suppresses their strengths (to a few meV). Because of reduced screening in the layered vdW structures, the density-density Coulomb interactions are nonlocal and show a long-ranged tail. The latter is visible in Table I by comparing the local interactions U_0 to the nearest-neighbor ones in both in- and out-of-plane direction. In contrast to the out-of-plane hopping matrix elements, we do not see a significant bilayer hybridization effect in the nonlocal density-density Coulomb interactions. Comparing $U_\perp^{(s)}$ and $U_\perp^{(w)}$, we find only small differences, which can be explained by the slightly different distances between the molecular orbital centers in these two directions.

Comparing the bulk parameter with the mono- and bilayer ones, we do not see sizable differences in the hopping parameter and only mild enhancements of the bare interactions, but strong enhancements of the *screened* Coulomb matrix elements. The latter is mostly driven by the *reduced* screening in the mono- and bilayer limit as compared to the bulk structures, as clearly visible from the reduced ε_{eff} in these structures. Thus, while the bulk and bilayer structures behave rather similar in terms of their non-interacting electronic structure, they could be vastly different as a result of different screening environments.

Taken together, our *ab initio* downfolding calculations show that the local Coulomb interactions U_0 are very large in comparison to in-plane hopping terms with $U_0/t_\parallel$ ratios always larger than 80. In comparison to the strong out-of-plane hopping matrix elements, we find $U_0/t_\perp^{(s)}$ ratios that decrease from about 12 in Nb_3Cl_8 to around 4 in Nb_3I_8. These ratios point towards possible strong Coulomb-interaction induced correlation effects, which might change from system to system. To investigate this and quantify the correlation strengths, we proceed with solving the generalized Hubbard models using cluster dynamical mean-field theory.

D. Generalized phase diagram from cluster dynamical mean field theory at half-filling

1. Self-energies

Using our cRPA-based downfolded molecular-orbital models, we calculate the self-energies at half-filling within dynamical mean-field theory (DMFT) and its Hubbard-I approximation [52,53]. Specifically, we solve the two molecular-orbital impurity problem, with the orbitals being centered at neighboring layers. We include all downfolded hopping matrix elements and all local intradimer Coulomb interaction elements U_{ijkl}. Accordingly, we deal with a cluster DMFT problem [19,54,55]. Figure 6 shows the resulting cluster DMFT Matsubara frequency self-energies in the diagonal $\psi^{(\pm)}$ basis for all compounds calculated using a CT-HYB quantum Monte Carlo solver at $\beta = 100\ \mathrm{eV}^{-1}$ (see Sec. V A for all details). In this basis at half-filling, the imaginary parts of the self-energy are the same for both channels ($\mathrm{Im}\,\Sigma_{(+)} = \mathrm{Im}\,\Sigma_{(-)}$), while the real parts differ only in their signs ($\mathrm{Re}\Sigma_{(+)} = -\mathrm{Re}\Sigma_{(-)}$) in the case of Cl, Br, and I. For $Nb_3F_8^*$ the bonding and antibonding self-energies lie on top of each other in Fig. 6.

The real part, as depicted in Fig. 6(a), shows that correlation effects enhance the bonding-antibonding splitting, similar to the Stoner enhancement of the exchange splitting in magnetic systems. In I, the real part is almost frequency independent, while it becomes strongly frequency dependent moving towards Cl. This is a sign of the increasing importance of dynamic correlation effects, which necessitate (cluster) DMFT calculations. In the imaginary part depicted in Fig. 6(b), we again find a clear trend: the overall amplitudes of the self-energy gradually increase from I to Br, Cl, and F, which is another sign of the increasing degree of correlation. Specifically, we see that the imaginary part of the self-energy of Nb_3I_8 is barely changing with frequency, while it clearly shows retardation effects in Nb_3Cl_8 and Nb_3Br_8. Finally, $Nb_3F_8^*$ shows a divergent imaginary self-energy for small Matsubara frequencies.

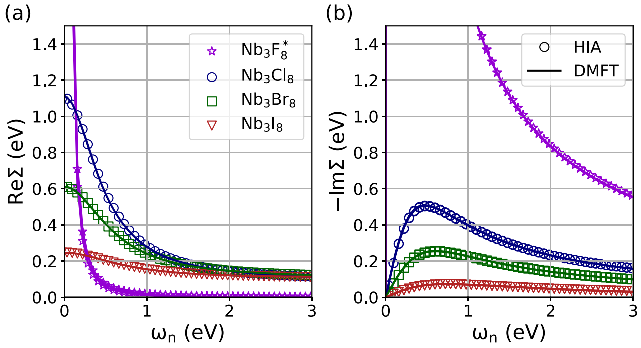

FIG. 6. LT ($R\bar{3}m$) Nb_3X_8 Matsubara self-energies. (a) Real and (b) imaginary parts of the self energies in Matsubara frequencies in the bonding-antibonding basis. Markers represent Hubbard-I results, lines represent cluster DMFT results.

Since in Nb_3I_8 retardation effects are vanishingly small, while its $\mathrm{Re}[\Sigma(i\omega_n)] > 0$, we can classify Nb_3I_8 as a weakly correlated dimerized (or obstructed atomic) band insulator. Nb_3Br_8 and Nb_3Cl_8 in turn show signatures of strongly correlated insulators, while $Nb_3F_8^*$ behaves like a conventional Mott insulator [25].

2. Phase classification based on local molecular dimer properties

To further substantiate this classification of LT bulk Nb_3X_8 into Mott, strongly and weakly correlated insulators, we proceed with analyzing the “local impurity,” i.e., the dimer formed by the hybridized molecular orbitals from adjacent monolayers, in more detail. This is similar to the analysis by Zhang *et al.* [22]. However, we use here our material-specific model parameters and, importantly, the full Coulomb tensor including nonlocal interactions between the molecular orbital sites (which is important for charge-neutral excitations [56]) to not only calculate $T = 0$ properties, but also finite temperature expectation values.

The dimer ground state is characterized by a multireference Slater determinant of the form $\alpha(|\uparrow,\downarrow\rangle - |\downarrow,\uparrow\rangle) + \beta(|\uparrow\downarrow,.\rangle - |.,\downarrow\uparrow\rangle)$, while the first charge-neutral excitations can be described by the triplet $\{|\uparrow,\uparrow\rangle, |\downarrow,\downarrow\rangle, |\uparrow,\downarrow\rangle + |\downarrow,\uparrow\rangle\}$ and a charge excitation of the form $|\uparrow\downarrow,.\rangle - |.,\downarrow\uparrow\rangle$.

In Fig. 7 we analyze and compare the ground and excited states among all compounds. At low temperatures, we find that the double occupation $\langle n_{\uparrow 0} n_{\downarrow 0}\rangle$ of $Nb_3F_8^*$ is nearly fully suppressed, while it is small but finite in Nb_3Cl_8 and Nb_3Br_8 and finally rather large in Nb_3I_8. This results from the large $U_0/\tau_\perp$ ratio in $Nb_3F_8^*$, which basically prohibits two electrons of different spins to be in the same molecular orbital. In turn, for Nb_3I_8 this ratio is strongly reduced, such that a double occupation is possible. This trend continues in the charge-neutral excitation energies. We see that the spin-excitation gap of the $Nb_3F_8^*$ dimer is vanishingly small, while it is small but finite for Nb_3Cl_8 and Nb_3Br_8, and finally rather large in Nb_3I_8. The charge-excitation energy in turn decreases from $Nb_3F_8^*$ to Nb_3I_8, such that the excitations are energetically orders of magnitude apart in $Nb_3F_8^*$ and of the same order in Nb_3I_8.

This zero temperature analysis thus clearly separates $Nb_3F_8^*$ from the others, which underlines its special status

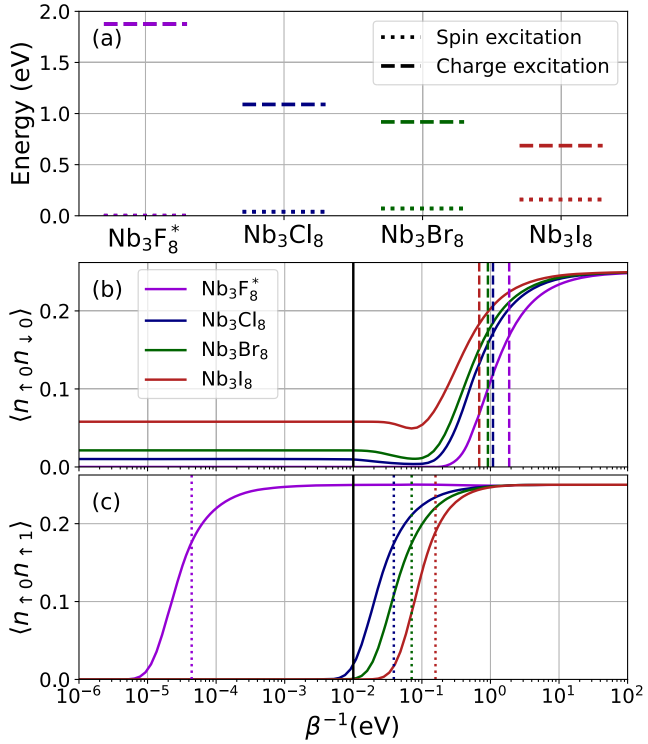

FIG. 7. Local dimer analysis with parameters from downfolded LT ($R\bar{3}m$) Nb_3X_8 models. (a) The charge neutral excitation spectrum. (b) and (c) The temperature dependence of double occupation $\langle n_{0,\uparrow} n_{0,\downarrow} \rangle$ and interlayer spin alignment $\langle n_{0,\uparrow} n_{1,\uparrow} \rangle$. These can be interpreted as measures for the thermal occupation of the first charge and spin excitation, respectively, as indicated by the characteristic temperatures $T_c = E_{\mathrm{exc}}/k_b$, plotted as dotted or dashed lines. The black line is the temperature at which we perform our DMFT study $\beta = 100\ \mathrm{eV}^{-1}$.

as a conventional Mott insulator. The difference between Nb_3Cl_8/Nb_3Br_8 and Nb_3I_8 is more quantitative, but due to their vastly different material parameters still obvious. In fact, Nb_3Cl_8/Nb_3Br_8 and Nb_3I_8 are that much different that we find for Nb_3I_8 a perturbative *GW*-like description to be perfectly adequate, while it breaks down in Nb_3Cl_8 and Nb_3Br_8, as discussed in more detail in Appendix A 2. Taking this and the self-energy property discussion together, this justifies differentiating Nb_3Cl_8/Nb_3Br_8 and Nb_3I_8 into strongly and weakly correlated insulators.

Finally, as a result of the similar spin and charge excitation energies, we find the spin and charge excited states to get partially occupied in Nb_3I_8 at rather similar temperatures, while these temperature scales are (very) different in the other compounds, cf. Figs. 7(b) and 7(c). Moreover, we find the (lower) spin excitation to be thermally activated in Nb_3Br_8 and Nb_3Cl_8 only at temperatures in which these compounds are already in their high-temperature phases. As such the temperature response of $Nb_3F_8^*/Nb_3Br_8/Nb_3Cl_8$ and Nb_3I_8 are vastly different.

3. *Momentum-resolved spectral functions*

Next to the dimer-local charge-neutral excitation spectra, charged excitations, such as measured by ARPES, can give further insights into the differences between the four compounds. To this end we study in the following the full lattice spectral functions $A_k(\omega)$, which we can easily access via the so-called Hubbard-I approximation [52]. This approximation should be in good agreement with our full cluster DMFT results at integer fillings due to the very large U_0 compared to the hopping to the bath (i.e., $t_\perp^{(w)}$, $t_\parallel$) for all systems. This assumption is confirmed by the self-energy results shown in Fig. 6. Importantly, the Hubbard-I approximation gives us direct analytic access to real-frequency retarded spectral functions.

The fully interacting spectral functions $A_k(\omega)$ for all four compounds at half-filling ($N_e = 2$ reflecting the number of electrons in the two flat bands formed by the molecular orbitals) are shown in Figs. 8(a)–8(d). In all cases, we see that the gap is widened in comparison to the mean-field DFT solutions shown in Fig. 4. For Nb_3Cl_8, Nb_3Br_8, and Nb_3I_8, we see additional flat features at lower and higher energies [indicated by blue arrows in Figs. 8(c)–8(d)], which are most strongly separated in energy for Nb_3I_8, less and less in Nb_3Cl_8 and Nb_3Br_8 until they are merged with the main features in the case of $Nb_3F_8^*$.

Upon analyzing the exact diagonalization results of the generalized Hubbard dimer, which serves as the origin of the Hubbard-I self-energies (see Appendix A 2 for details), we understand that, indeed, in $Nb_3F_8^*$ a conventional Mott gap is formed. $Nb_3F_8^*$ is thus a half-filled two-band Mott insulator, see Fig. 8(a). In Nb_3Cl_8 and Nb_3Br_8, the gap is formed between a lower Hubbard band (LHB) of the bonding orbital and the upper Hubbard band (UHB) of the antibonding orbital, which is further accompanied by a secondary LHB of the antibonding orbital (below the LHB of the bonding orbital) and a secondary UHB of the bonding orbital (above the UHB of the antibonding orbital), see Figs. 8(b)–8(c). This is not in line with the conventional Mott insulator characterization, but shares strongly retarded self-energies as a common origin as shown in Appendix A 8. As such, classifying both Nb_3Cl_8 and Nb_3Br_8 as strongly correlated insulators is appropriate. In Nb_3I_8 all strong correlation (retardation) effects are significantly suppressed, such that the gap is best understood as being formed between the original bonding and antibonding bands, but slightly enhanced by Coulomb interactions, see Fig. 8(d). Nb_3I_8 is thus indeed best classified as a weakly correlated band insulator. This is in qualitative agreement with the bilayer studies by Hu *et al.* [57] and Zhang *et al.* [22]. However, due to the lack of consistent material-specific model parameters for bilayer Cl and Br in their LT phases, Zhang *et al.*, came to the conclusion that Cl is a Mott insulator, while Br has been labeled a band insulator. Altogether, we again find clear

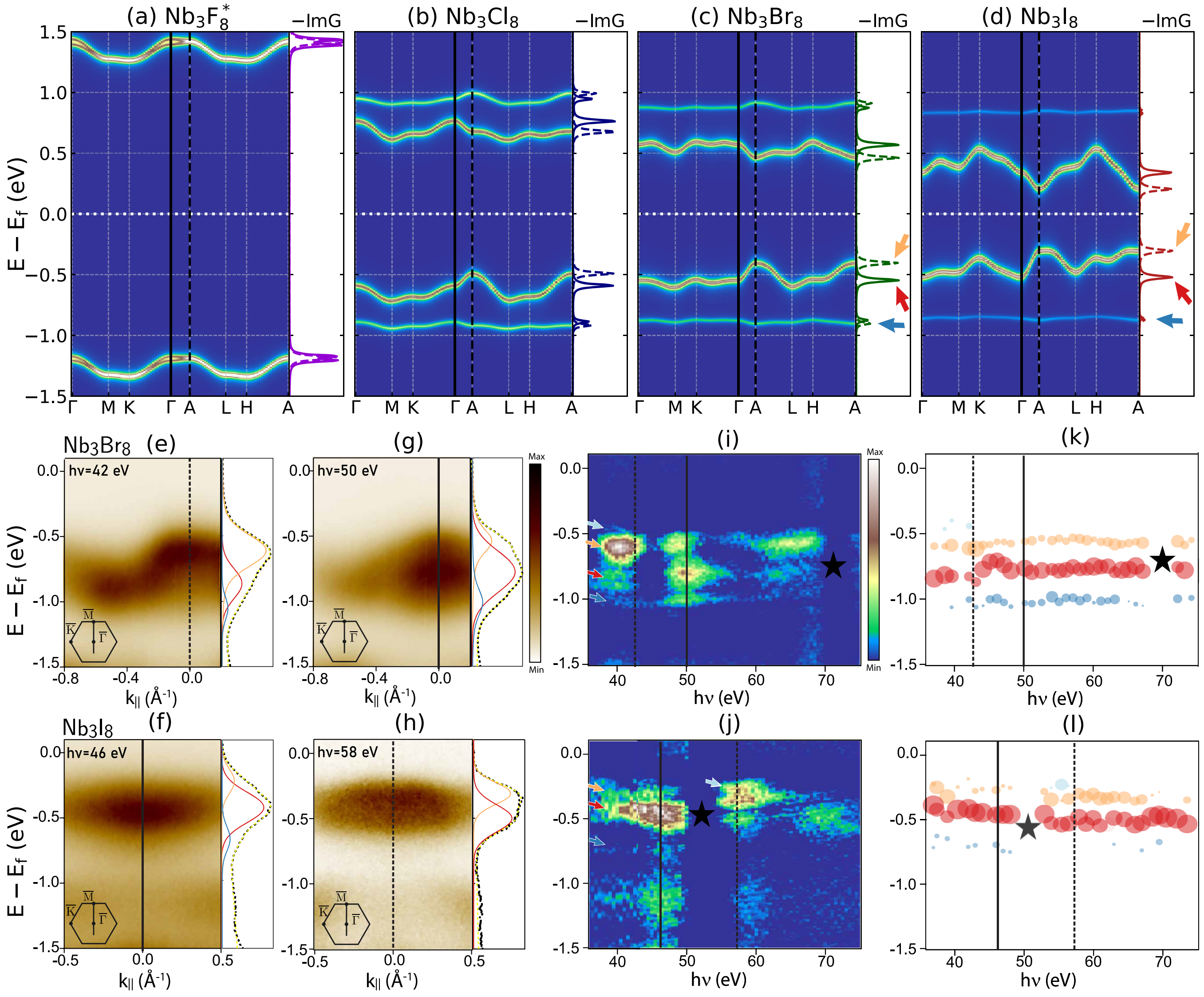

FIG. 8. Theoretical and experimental spectral functions of LT ($R\bar{3}m$) Nb_3X_8 at half-filling ($\mathbf{N_e} = \mathbf{2}$). (a)–(d) Momentum resolved spectral functions within Hubbard-I approximation. Line cuts at Γ and *A* are shown in full and dashed lines, respectively. (e)–(h) Raw ARPES data along $\bar{\Gamma} - \bar{M}$ alongside energy distribution curves (EDCs) taken at $\bar{\Gamma}$. (i)–(j) 2D curvature plots of EDCs plotted against photon energy. (k)–(l) EDC position and normalized area from curve fits using Voigt function at each photon energy. Dot sizes represent the normalized area under the curve. Dashed and solid lines in (i)–(k) and (j)–(l) connect to photon energies indicated in (e)–(g) and (f)–(h), respectively. Arrows in (i)–(j) indicate features matching curve fits in (k)–(l) and are associated with features marked by the same arrows in (c) and (d).

trends going from $Nb_3F_8^*$ to Nb_3I_8: the fundamental gap decreases and the energetic separation of the secondary LHB/UHB features increases, while their spectral weights vanish towards Nb_3I_8.

Experimentally, the fundamental gaps of Nb_3X_8 have not yet been studied in great detail. To our knowledge, only Nb_3Cl_8 has previously been studied in absorption, photoluminescence, and transport measurements, indicating a gap size of about 1.1 eV [23,26,36,45], which is in good agreement with our theoretical prediction of an indirect gap of about 1.11 eV [see Fig. 8(b)].

4. *Strong correlation features uncovered by angle-resolved photoemission spectroscopy*

We note that the secondary LHB/UHBs in the LT bulk structures, which are most prominent in Nb_3Cl_8 and Nb_3Br_8, are only captured by *cluster* DMFT calculations. Using a *single-site* DMFT approximation, as we previously applied for bulk Nb_3Cl_8 [24] and as applied in other studies [23], these features are much more coherent and even above and below the primary LHB/UHBs, as further detailed in Appendix A 3. This underlines the importance of two-site cluster DMFT calculations for the LT structures, which take the full matrix structure of the self-energy (from the two orbitals depicted in Fig. 5) into account. We further note that our fully momentum dependent highly resolved low-temperature real-frequency Hubbard-I spectral functions $A_k(\omega)$ uncovers an intriguing difference between the primary (bonding) and the secondary (antibonding) lower Hubbard bands: the primary (bonding) one still disperses (most prominently between Γ and A), while the secondary (antibonding) one is nearly dispersion-less.

Thus, from ARPES measurements performed in normal emission geometry, which measure $A_k(\omega)$ along Γ-A, we should naively expect a feature with a clear k_z dispersion, representing the primary (bonding) LHB between Γ and A, as well as a minor and less dispersive structure stemming from the secondary (antibonding) LHB. Note, however, that ARPES is a surface sensitive technique and the localization of the photohole can lead to a strong smearing in k_z, rendering the actual observation less clear.

To explore the manifestation of the many-body effects in the spectral function experimentally, we have performed ARPES experiments on Nb_3Br_8 and Nb_3I_8 (see Methods Sec. V E and Appendix A 11 for more details). Consistent with the literature [23,25,35–37], we see that the upmost occupied band shows a splitting for these compounds, which is especially visible around $\bar{\Gamma}$, see Figs. 8(e)–8(l). We argue that this splitting actually reflects the expected three-dimensional character of the primary (bonding) LHB band and we also find spectroscopic evidence for the less dispersive and weaker secondary (antibonding) LHB.

We focus our analysis on data collected in normal emission (at $\bar{\Gamma}$), corresponding to the bulk A-Γ-A high-symmetry direction. This is accomplished by measuring the photoemission intensity as a function of photon energy, which corresponds to a variation in k_z. Figures 8(e)–8(h) show the photoemission intensity for Nb_3Br_8 and Nb_3I_8 along the $\bar{\Gamma}-\bar{M}$ direction of the surface Brillouin zone at different photon energies. Also shown are energy distribution curves (EDCs) at $k_\parallel = 0$ (normal emission). These EDCs form the basis of the photon energy-dependent photoemission intensity which is shown in Figs. 8(i)–8(j) as a curvature plot. The main features in the EDCs and in the photon energy-dependent intensity are two intense peaks. For Nb_3Br_8, a third minor peak is strictly required to obtain a good fit to the data; for Nb_3I_8 we also include such a third peak in EDC fits but it is found to be very weak throughout the range of investigated photon energies. The resulting fits to three Voigt lines are also shown in Figs. 8(e)–8(h). For now, we focus on the two intense peaks. The intensity of lower (higher) peak reaches a maximum at the photon energies corresponding to the bulk Γ (A) points, as marked by red (orange) arrows in Figs. 8(i)–8(j) and the corresponding dots in Figs. 8(k)–8(l). We interpret these peaks not as two separate bands but rather as the extrema reached in the dispersion of the primary (bonding) LHB between the bulk Γ and A points. Such interpretation is consistent with the fact that the high density of states at the extrema of a one-dimensional dispersion probed in normal emission can be expected to dominate the photoemission intensity in the presence of k_z broadening. There are many examples of such behavior in the literature, e.g., in the case of the noncorrelated topological insulator Bi_2Se_3, see Fig. 6 in Ref. [58]. In this interpretation, the separation between the peaks of 0.25 eV and 0.19 eV for Nb_3Br_8 and Nb_3I_8, respectively, can be interpreted as the total bandwidth along the Γ-A direction. This is in good qualitative agreement with our theoretical estimates for these k_z bandwidths, as indicated by the spectra taken at Γ and A, shown in the side panels of Figs. 8(c) and 8(d). We note that these bandwidths are mostly defined by the underlying PBE functional based on which our cluster DMFT calculations are performed. Correlation-driven renormalizations are on the order of 30 to 50 meV and thus play only a minor role.

We now return to the fact that a good fit for the EDCs from Nb_3Br_8 requires taking a third feature at lower energies into account. Figures 8(k)–8(l) show how the fitted peak positions and relative areas develop with photon energy. The third minor peak in the fits [marked by the blue arrow in Fig. 8(i) and blue dots in Fig. 8(k)] is strictly needed to obtain good fits for Nb_3Br_8 and the resulting band has a strongly suppressed dispersion and spectral weight. Based on these properties we interpret this as the secondary LHB of the antibonding orbital. We note that this feature might also be present in the EDCs by Date *et al.* [25]. In contrast, for Nb_3I_8 this third feature is not strictly needed to obtain a satisfactory fit to the EDCs. It is very weak in the 46 eV data and it is absent in the 58 eV data, see Figs. 8(f) and 8(h). This is in agreement with our cluster DMFT calculations that predict a significant spectral weight reduction of the secondary LHB in Nb_3I_8 compared to Nb_3Br_8.

We thus stress that the presence of two resonances, which has been argued to be a hallmark of (strong) correlation effects [22,23], is not sufficient to unambiguously differentiate between a conventional band, a strongly correlated band, and a Mott insulator based on ARPES data, as it results from the k_z dispersion of the upmost occupied band, which is present even without correlation effects. While Date *et al.* [25] argue that the details of this k_z dispersion is altered by strong correlation effects, we instead suggest to search for the existence of the third resonance at slightly lower energies resulting from the secondary LHB. This is a clear and unambiguous feature of strong correlation effects in the strongly correlated insulators in their LT phases resulting from Coulomb driven retardation properties.

Finally, we note that further comparison with the available ARPES results shows that the lower t_{2g}^2 bands, which we neglect within our cluster DMFT calculations, are still separated from the upmost bands by about

0.5 to 1 eV (increasing from I to Br), which is in agreement with the trends expected from comparison to DFT calculations, ruling out charge-transfer insulating states.

From this analysis we conclude that also charged excitations, as measured by photoemission spectroscopes, are adequate probes to observe the qualitative and quantitative differences between the four compounds.

5. Combined phase diagram

To organize the four different compounds of the whole Nb_3X_8 material class, including their monolayer, bilayer, and bulk structures, in both low- and high-temperature phases, we propose to position each system into a plane spanned by the inverse in- vs out-of-plane correlation strengths. The inverse in-plane correlation strength can be measured by the ratio of the in-plane hopping $\tau_\parallel = |t_\parallel|$ to the local cRPA screened Coulomb interaction U_0, as $t_\parallel$ dominates the in-plane kinetics in all systems. The inverse out-of-plane correlation strength can be measured by the ratio of the out-of-plane dimerization strength to U_0. The dimerization strength can be conveniently characterized by the single-particle gap of the local dimer as approximated by $\tau_\perp = |t_\perp^{(s)} - \sqrt{3} t_\perp^{(w)}|$ in the LT phase. In the HT (monolayers) structures this is approximately (by definition) zero and for LT (HT) bilayers given by $\tau_\perp = |t_\perp^{(s/w)}|$. This extends and generalizes the schematic phase diagram by Date *et al.* [25] and the simplified one by Zhang *et al.* [22]. Importantly, our proposal uses appropriately normed ratios and is based on all relevant material properties including the local Coulomb strengths U_0 as well as the out-of- and in-plane hoppings $t_\perp^{(s)}$, $t_\perp^{(w)}$, and $t_\parallel$. This way, we can consistently organize all materials in all structures in one and the same phase diagram.

The result is presented in Fig. 1 for which we used our material-specific parameters from Table I. This way, the pure (single or two band) Mott insulators are all positioned on the bottom of the phase diagram. Their positions on the horizontal in-plane correlation strength axis changes, with monolayer Nb_3Br_8 being the strongest Mott insulator (due to the weakly screened U_0 and small $\tau_\parallel$) and LT bulk $Nb_3F_8^*$ the weakest Mott insulator (due to its relatively large $\tau_\parallel$). It is worth pointing out that in terms of in-plane correlation Nb_3Br_8 and Nb_3I_8 break the trend following the order of the periodic table. This is caused by $\tau_\parallel$ being smallest in Nb_3Br_8. Most of the LT bilayer and all thicker Nb_3Cl_8 and Nb_3Br_8 systems lie above the boundary in the correlated insulator phase, mostly driven by rather large out-of-plane dimerization strengths as a result of small dimerization gaps and large Coulomb repulsions. LT bulk Nb_3I_8 is positioned in the band insulator phase as a result of a large dimerization strength and rather weak (strongly screened) local Coulomb interaction. Upon thinning LT Nb_3I_8 down from the bulk to a bilayer structure, which barely affects the in-plane hopping or the out-of-plane dimerization strengths, the LT bilayer Nb_3I_8 nevertheless behaves fundamentally different (as a correlated insulator) as a result of the drastically enhanced local Coulomb interaction due to the reduced screening in the bilayer structure.

Based on our phase classification discussion from above, we note that we expect the transition from a Mott to a correlated insulator to happen rather abruptly (as it is accompanied by clear qualitative differences, e.g., in the self-energies), while the transition from correlated to band insulators is more continuous. We furthermore expect that the phase boundaries are not only controlled by the out-of-plane correlation strengths, but also by the in-plane one. This is reflected by taking the critical $t_\parallel/U_0$ ratio for the Mott transition in triangular lattices as found by Ref. [59] into account here.

Most importantly, this generalized phase diagram gives a clear guidance into which direction a system changes. For example, upon applying pressure the in- or out-of-plane hopping likely increase such that a Mott insulator might be tuned to a correlated insulator or a correlated one into a conventional band insulator. Similarly, decreasing the Coulomb interaction, e.g., in bilayer systems via external screening, can tune the material through the same phases, but affecting simultaneously the in- and out-of-plane correlation strengths. This way this phase diagram clearly shows that uniaxial in- or out-of-plane strain or stress affects the material at hand differently than external screening. Also, from this it becomes clear why all monolayer as well as HT bulk Nb_3X_8 systems will be Mott insulators: in all of them the out-of-plane correlation strengths is zero (or strongly suppressed), while the in-plane one is still large as a result of small $t_\parallel$ and (rather) large U_0.

E. Dynamical lattice stability and electron-phonon coupling to low-energy subspace

So far, we showed that the low-energy electronic structure of all compounds will be renormalized by the Coulomb interactions. Together with the inclusion of the so-far only putative $Nb_3F_8^*$ structure, this raises questions about the dynamical stability of the underlying LT bulk crystal structures. To address this, we performed density functional perturbation theory (DFPT) calculations for all compounds (see Methods for computational details).

The resulting low-energy phonon dispersions for bulk LT Nb_3X_8 are shown in Fig. 9 and full dispersions can be found in Appendix A 5. We see that within DFPT all compounds are dynamically stable, even the new putative $Nb_3F_8^*$. From Nb_3I_8 to $Nb_3F_8^*$, we see clearly how the phonon spectra get stiffer as a result of the decreasing lattice constant, cf. Table I. This trend is in line with previous phonon calculations for the monolayer compounds [60,61]. We also note that the monolayer and bilayer LT structures are dynamically stable in our calculations (see Appendix A 5)

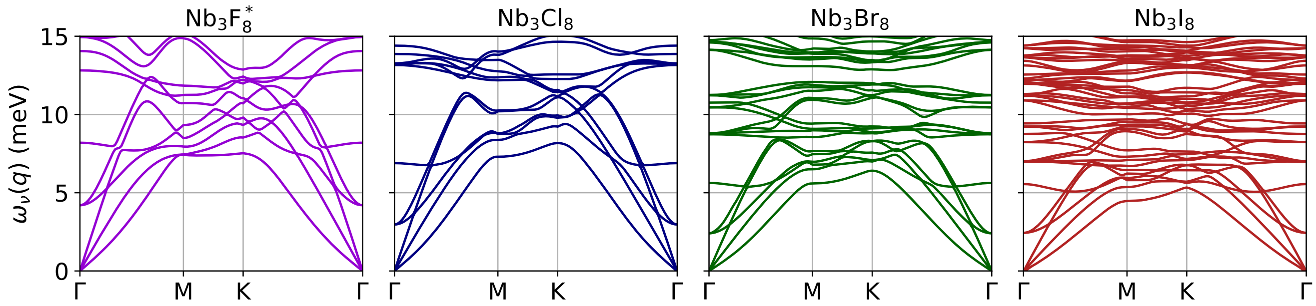

FIG. 9. Phonon spectra of LT ($R\bar{3}m$) bulk Nb_3X_8. From left to right $Nb_3F_8^*$, Nb_3Cl_8, Nb_3Br_8, and Nb_3I_8 calculated using density functional perturbation theory.

and that the monolayer phonon dispersions are in good agreement with previous data [21,60,61].

While this is a promising result, we need to reflect on the applicability of DFPT in the presence of (strong) Coulomb correlation effects. Specifically, the corresponding renormalization effects to the electronic structures are not present on the DFT level, which has been used to relax all structures and which is used to perform the perturbation calculations within DFPT. Thus, it is *a priori* not clear how reliable the DFT optimized lattice structures and the presented phonon dispersions are. To investigate this, we additionally performed so-called constrained DFPT (cDFPT) [62,63] calculations for $Nb_3F_8^*$ and Nb_3Cl_8, which allows us to calculate the phonon spectra upon removing all electron-phonon couplings to the low-energy electronic structure. Therefore, the (most strongly) renormalized parts of the electronic structure are effectively disregarded within cDFPT.

Comparing the DFPT and cDFPT phonon spectra of $Nb_3F_8^*$ and Nb_3Cl_8 in Appendix A 6, we see that the coupling to the low-energy electronic states barely changes the phonon energies. This is an important result, as it shows that the phonons are weakly coupled to the low-energy electronic states. Therefore, it is reasonable to assume that beyond-DFT corrections to this electronic subspace do not affect the dynamical stability, and that our relaxed structures and the resulting DFPT phonon spectra are trustworthy.

F. Doping effects

The study of doping provides a way to differentiate between strongly and weakly correlated insulators. In conventional weakly correlated band insulators, electron or hole doping just yields a shift in the chemical potential while the band structure does not change. In contrast, strongly correlated insulators can show entirely new electronic features, such as Kondo resonances [64], upon doping.

1. Integer doping ($N_e = 3$)

We begin with doping the system by exactly one electron per dimerized inter-layer trimer. In this case we still deal with integer filling of the two flat bands, but with $N_e = 3$ instead of half filling with $N_e = 2$, such that we can still use the Hubbard-I approximation. The resulting doped spectral functions are shown in Fig. 10. From a pure band-structure perspective, we would expect that doping the systems with

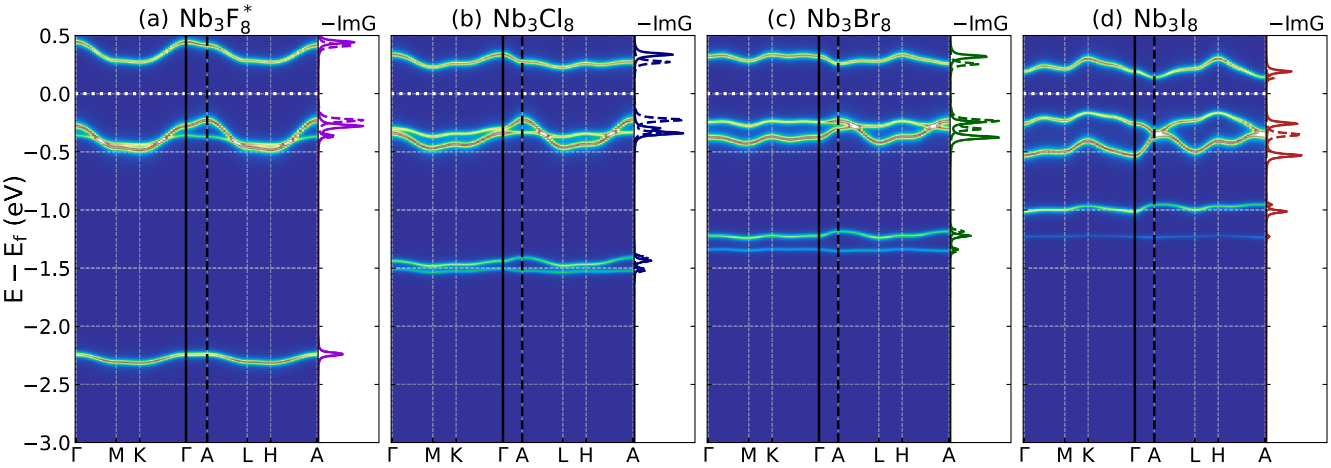

FIG. 10. Theoretical spectral functions of LT ($R\bar{3}m$) Nb_3X_8 at $\mathbf{N_e} = \mathbf{3}$. (a)–(d) Interacting spectral functions of doped compounds calculated using the Hubbard-I approximation. Line cuts at Γ and A are shown in full and dashed lines, respectively.

one electron (or equivalently one hole), would just half-occupy the noninteracting antibonding (bonding) band, making all systems good metals. Instead, we find that *all systems* have a gap of around 0.5 eV, which we understand as clear evidence for strong correlation effects developing in all systems, including Nb_3I_8. In detail, by doping with only one electron (hole), $Nb_3F_8^*$ and Nb_3Cl_8 are now strongly correlated charge transfer insulators (see overlap between the new uncorrelated bonding bands and the lower Hubbard band of the antibonding band), while Nb_3Br_8 and Nb_3I_8 are now Mott insulators. In all cases the gaps are opened by strong retardation effects of the self-energy as we explain in more detail in Appendix A 8. Taking the approximate particle-hole symmetry of the flat noninteracting bonding or antibonding bands into account, we expect that doping in the other direction, to $N_e = 1$, yields similar correlated electronic structures. Experimentally, this could be achieved by replacing one halide with one chalcogen atom per dimerized unit cell, e.g., within $Nb_3X_{7.5}Te_{0.5}$. We note that Refs. [65,66] find Nb_3Cl_7Te and Nb_3I_7Te still displaying the breathing mode kagome lattice, respectively, indicating the stability of the lattice even under higher doping.

We further note that for $N_e = 3$, the nonlocal (density-density) Coulomb interaction is now playing a quantitatively important role by strongly increasing the gap. If we neglect this contribution, the strongly correlated gaps are much smaller (see Appendix A 4). This once again stresses the relevance of having access to all material-specific parameters, including the nonlocal Coulomb interactions.

2. Continuous doping ($N_e = 2 + \delta$)

To analyze the details of the changes from $N_e = 2$ to $N_e = 3$, we performed additional calculations for the Cl, Br, and I compounds at various doping levels in between denoted by $N_e = 2 + \delta$. In these cases Hubbard-I is not a good approximation any more, such that we are restricted to imaginary time or frequency cluster DMFT and corresponding quantum Monte Carlo calculations (see Methods for details). The resulting imaginary frequency self-energies are discussed in Appendix A 7. In the bonding orbital channel we find for small dopings δ stronger dynamic correlation effects in Nb_3Cl_8 and Nb_3Br_8 compared to Nb_3I_8, which become rather weak for all materials toward $N_e = 3$. The antibonding self-energy behaves oppositely for all systems. Upon increasing the doping from $N_e = 2$ to $N_e = 3$, dynamic correlations generally increase. This is also reflected in the orbital-dependent quasiparticle weights, which we extracted from the imaginary frequency self-energies and show in Fig. 11(a). The bonding quasiparticle weights of Nb_3Cl_8 and Nb_3Br_8 start close to zero in the vicinity of $N_e = 2$, indicative of strong correlation effects, and steadily increase with doping, while for Nb_3I_8 it is larger than 0.5 at all fillings, indicative of moderate correlation effects. On the other hand, the antibonding orbital quasiparticle weight drastically decreases towards $N_e = 3$ for all three compounds. This can be understood from the band perspective, where $N_e = 3$ corresponds to a half-filled antibonding band. The large Coulomb interaction compared to the kinetic energy thus renders the $N_e = 3$ systems more or less conventional single-band Mott insulators, but with a lower Hubbard band that is close to the fully occupied and now less correlated bonding band.

To gain further spectroscopic insights into the continuous doping responses of the systems, we continued our imaginary frequency data to the real axis. To this end, we apply the recently proposed minimal pole representation method [67,68] to analytically continue the matrix-valued local self-energies and calculate from this the interacting

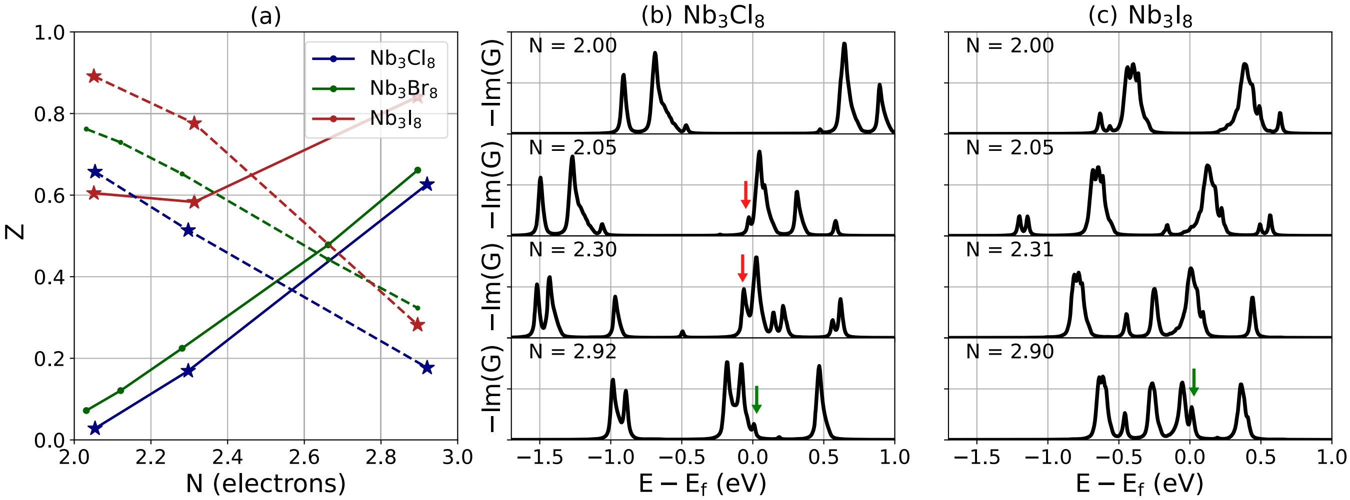

FIG. 11. Doping dependence of LT ($R\bar{3}m$) Nb_3X_8. Behavior under doping of (a) the quasiparticle weight of the bonding (solid) and antibonding (dashed) components and the analytically continued local spectral functions of (b) Nb_3Cl_8 and (c) Nb_3I_8. Stars in (a) indicate doping levels, which are analyzed in (b) and (c).

local spectra for Nb_3Cl_8 and Nb_3I_8. We chose the latter two to highlight the differences between the doping dependence of a strongly and a weakly correlated system. The results are shown in Figs. 11(b) and 11(c). For Nb_3Cl_8 starting with a small doping of $\delta = 0.05$, we see that the main features shift and, importantly, a small resonance at $\omega = 0$ eV arises, which grows in intensity towards $\delta = 0.3$, as indicated by the red arrows in Fig. 11(b). This is reminiscent of a Kondo resonance, which is a hallmark of doped strongly correlated insulators. Simultaneously, we see that at higher energies new resonances appear, which form at large dopings ($\delta = 0.92$) a new upper Hubbard band. In fact, we can understand the Nb_3Cl_8 $\delta = 0.92$ data as a slightly hole-doped variant of the $N_e = 3$ situations, which already shows the single-orbital lower and upper Hubbard bands, but here, due to finite hole doping, accompanied by a Kondo resonance, as indicated by the green arrow in Fig. 11(b).

In contrast, the Nb_3I_8 spectra more or less just shift in energy until around $\delta = 0.3$, without introducing any new features and especially without showing any evidence of a Kondo resonance at zero energy. This is the doping dependence we expect from conventional weakly correlated band insulators. However, for larger dopings, we start to see new features, which are in line with our interpretation of Nb_3I_8 as a single-band Mott insulator at $N_e = 3$. In detail, at $\delta = 0.9$ we should understand Nb_3I_8 as a hole-doped single-band Mott insulator showing a Kondo resonance, cf. green arrow in Fig. 11(c).

G. Magnetic properties of monolayer and bulk Nb_3X_8

Magnetism is a ubiquitous concept in correlated materials and has received considerable attention in Nb_3X_8 as well. For the Nb_3Cl_8 monolayer, our previous work [24] and recent spin-spiral DFT [28] calculations both show a magnetically ordered state with 120° angles between trimer-centered moments. For the bulk LT phase, on the other hand, out-of-plane dimerization can lead to singlet formation [22,23,29,32,39], which is common in bilayer Hubbard models at large U and large $t_\perp/t_\parallel$ [57,69,70].

Although a detailed account of the quantum magnetism in Nb_3X_8 is beyond the scope of this work, it is insightful to study the connection between the magnetic, electronic, and lattice structure that arise from our downfolded models. Given the dominance of the Coulomb interaction over the hopping matrix elements [e.g., for Nb_3Br_8 U^{eff} is approximately five (hundred) times larger than the largest out-of-plane (in-plane) hopping, see Table I], it is appropriate to describe the magnetic properties of Nb_3X_8 using a Heisenberg model that incorporates trimer-localized magnetic moments. Accordingly, we approximate the exchange interaction parameters $J_{ij} = -2(t_{ij})^2/U^{\mathrm{eff}}$ using the strong coupling expansion that incorporates the effective Coulomb interaction (see Sec. V C for details). This formulation indicates that the exchange interaction is strongest when the hopping matrix element between two sites is large, leading to antiferromagnetic (AFM) exchange interactions ($J_{ij} < 0$). This behavior is characteristic of materials with large U, such as all Nb halides, and explains the differences to DFT estimates that do not account for large values of U [28,71].

TABLE II. Effective exchange parameters $J^{(n)}$ (in meV) and ground state spin spiral periods $\lambda^{(n)}$ (in units of in-plane lattice parameter a) for ML Nb_3X_8. Here, $n = 1, 2, 3$ denotes the first, second, and third shells of nearest neighbors, with $n \leq 2$ and $n \leq 3$ indicating truncations for exchange interactions $J_{ij}^{(n)}$ to two and three shells, respectively.

	$Nb_3F_8^*$	Nb_3Cl_8	Nb_3Br_8	Nb_3I_8
$J^{(1)}$	−1.13	−0.63	−0.04	−0.40
$J^{(2)}$	0.00	−0.04	−0.06	−0.16
$J^{(3)}$	0.00	−0.03	−0.08	−0.26
$\lambda^{(n\leq 2)}$	$1.5a$	$1.5a$	$2.1a$	$1.7a$
$\lambda^{(n\leq 3)}$	$1.5a$	$1.5a$	$2.8a$	$2.3a$

Using our downfolded material-specific parameters from Tables I and IV, which includes appropriately screened nonlocal Coulomb matrix elements, we can thus calculate all (long-ranged) magnetic exchange interactions J_{ij} for all monolayer and bulk structures, see Tab. II and III, respectively. Afterwards, using either atomistic spin dynamics or classical Monte Carlo simulations (see Section V D), we solve the resulting Heisenberg Hamiltonian

$$H = -\sum_{i,j} J_{ij}\mathbf{S}_i \cdot \mathbf{S}_j - \sum_i \mathbf{B} \cdot \mathbf{S}_i, \qquad (2)$$

where the first term represents isotropic exchange interactions and the second term accounts for the Zeeman energy in the presence of an external magnetic field $\mathbf{B}$.

TABLE III. Effective exchange parameters for bulk Nb_3X_8 in the LT ($R\bar{3}m$) and HT ($P\bar{3}m1$) structure in meV. The labels (s) and (w) denote strongly and weakly bound neighbors in the out-of-plane ($\perp$) directions, respectively, while $n = 1, 2, 3$ corresponds to first, second, and third nearest neighbors in the in-plane ($\parallel$) direction. The last row presents the energies (in meV) associated with the magnetic ground state. For more details, see Appendix A 10.

	LT phase				HT phase	
	$Nb_3F_8^*$	Nb_3Cl_8	Nb_3Br_8	Nb_3I_8	Nb_3Cl_8	Nb_3Br_8
$J_\perp^{(s)}$	−0.03	−35.21	−67.98	−180.21	−0.55	−0.99
$J_\perp^{(w)}$	−0.04	−0.49	−0.98	−2.29	−0.48	−0.96
$J_\parallel^{(1)}$	−1.32	−0.83	−0.09	−0.26	−1.18	−0.30
$J_\parallel^{(2)}$	−0.00	−0.05	−0.07	−0.16	−0.05	−0.07
$J_\parallel^{(3)}$	0.00	−0.04	−0.10	−0.33	−0.04	−0.10
E_{ex}	−3.99	−37.61	−70.38	−185.98	−3.62	−3.94

1. Spin spirals in monolayer $\mathbf{Nb_3X_8}$

We first investigate the magnetic ground-state properties of Nb_3X_8 monolayers. Using the exchange interaction parameters provided in Table II, we solve Eq. (2) at $|\mathbf{B}| = 0$ using atomistic spin dynamics simulations. The results indicate that the ground states display spin spiral order across all Nb_3X_8. However, due to the finite size of the simulated structures, the resulting configurations yield commensurate spin spiral ordering. To address this, we analytically minimize the total energy given by the Hamiltonian from Eq. (2) with respect to the spin-spiral wave vector $\mathbf{q}$ assuming flat spirals (see Appendix A 10). The ground state periods of the spin spirals given by $\lambda = 2\pi/|\mathbf{q}|$ for various truncation distances between interacting effective spin pairs are given in Table II and further details can be found in Appendix A 10.

$Nb_3F_8^*$ and Nb_3Cl_8 exhibit identical spin spirals with a periodicity of $1.5a$, corresponding to a 120° antiferromagnetic (AFM) order, independent of taking the third nearest neighbor interaction into account or not. This changes for Nb_3Br_8 and Nb_3I_8. Notably, the relatively large $J^{(2)}$ for these compounds gives rise to incommensurate spin-spiral configurations, and when $J^{(3)}$ is taken into account, the modulation period increases further. These classical results are in good agreement with the quantum magnetic phase diagram presented by Gong *et al.* [72].

2. Out-of-plane magnetic frustrations as the origin of the lattice phase transition in bulk $\mathbf{Nb_3X_8}$

We proceed with the discussion the magnetic properties in both low- and high-temperature bulk structures as resulting from the magnetic interaction parameters given in Table III.

In bulk, The main difference between the LT and HT phases lies in the connectivity of the layers, as illustrated in Fig. 2(b). In the HT phase, every trimer is magnetically connected to three trimers in the layer above and three in the layer below by (rather small) $J_\perp^{(s/w)}$. As a result of the antiferromagnetic interlayer coupling, this leads to magnetic frustration in the HT structure: the trimer-moment cannot align consistently with all three moments in the upper and lower neighboring layers. On the other hand, in the LT phase, the dimerization in the vertical direction lifts this frustration and every trimer moment has another trimer moment to which it is coupled strongly by $J_\perp^{(s)}$, supporting singlet formation. Overall, this lowers the total energy of the system.

This is reflected in the total (magnetic) energies of Nb_3Cl_8 and Nb_3Br_8, which are reduced by about 34 and 66 meV in the LT phases, respectively (see Table III). This trend clearly correlates with the critical transition temperatures of Nb_3Cl_8 and Nb_3Br_8 [39] and offers a simple explanation of why Nb_3I_8, that has the largest exchange interaction energy among other LT Nb_3X_8 compounds, has so far been only observed in the LT phase. These observations made possible by our material-specific matrix elements are in line with the suggestion by Sheckleton *et al.* [32], that the interlayer magnetic frustration in the HT phase combined with energy gain due to singlet formation in LT phase drives the structural transition.

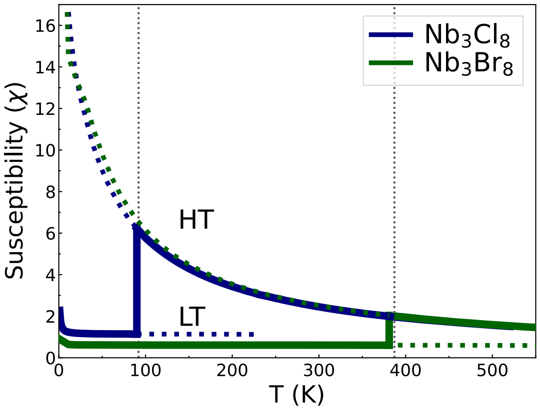

FIG. 12. Magnetic susceptibility of Nb_3Cl_8 and Nb_3Br_8. Classical Monte Carlo simulations of the magnetic susceptibility for both HT ($P\bar{3}m1$) and LT ($R\bar{3}m$) structures as a function of temperature T at magnetic field $B = 5$ T. The dotted vertical lines mark the transition temperatures at $T = 92$ and 387 K.

We note that in the case of LT $Nb_3F_8^*$, singlet formation is not energetically favorable. This is due to $J_\perp^{(\mathrm{s})} < J_\perp^{(\mathrm{w})} < J_\parallel^{(1)}$, which indicates that the primary contribution to the ground state arises from the in-plane 120°-AFM ordering.

This interpretation also aligns with the local magnetic susceptibilities, which we compute using classical Monte Carlo simulations (for computational details see Sec. V D) for Nb_3Cl_8 and Nb_3Br_8 in their LT and HT structures, solving Eq. (2) and considering a finite magnetic field. Indeed, as shown in Fig. 12, the computed magnetic susceptibilities for the HT structures of both Nb_3Cl_8 and Nb_3Br_8 match and follow a Curie-Weiss behavior. A concomitant collapse of the magnetic susceptibility accompanies the structural phase transition to the LT phase for both compounds. The reduction in magnetic susceptibility of LT Nb_3Br_8 compared to LT Nb_3Cl_8 can be attributed to a larger $J_\perp^{(\mathrm{s})}$, indicating that LT Nb_3Br_8 is less responsive to magnetic fields. This seems to be perfectly consistent with available experimental data [27,32–34,39,44] and recent analysis by Carta *et al.* [29]. However, we note that for fully compensated singlets, the susceptibilities in the LT phases should be completely suppressed, while our calculations show small but finite responses accompanied by small tails at low temperatures. These aspects necessitate further analysis, e.g. via full quantum mechanical treatments in the future.

H. Symmetry breaking in few-layer stacks and Connections to the field free Josephson diode effect

We now turn our focus to finite stacks of a few Nb_3X_8 layers and their potential role for the field-free Josephson diode effect. The latter, as observed in $NbSe_2/Nb_3Br_8/NbSe_2$ [30], requires simultaneous time-reversal (TRS) and inversion symmetry (IS) breaking [31,73].

The IS breaking can be straightforwardly discussed: Nb_3X_8 stacks with an even number of layers are inversion symmetric, while stacks with an odd number of layers break inversion symmetry. In particular, inversion symmetry is broken in the monolayer. The TRS breaking requires more attention, especially with respect to the impact of the dimerization (alternating hybridization) of bilayers, which depends on the number of involved layers. Specifically, there can be top and/or bottom surface layers that only weakly hybridize with their neighbor and can therefore approximately behave like freestanding monolayers. A trilayer, for example, consists of a dimerized bilayer accompanied by a nearly free monolayer, as depicted in Fig. 13. Taking the strong correlation effects into account, these surface monolayers realize (approximately) conventional single-band Mott insulators [74], which are only weakly coupled to the neighboring dimerized bilayer, as we show in more detail in Appendix A 9. In contrast, mean field DFT calculations, wrongly predict the trilayer to behave like a metallic monolayer in contact with a band-insulating bilayer, cf. Appendix 9 and Ref. [31]. Thus, in the context of symmetry breakings and the Josephson diode effect, correlation properties must be considered consistently throughout the whole structure with a special focus on unpaired surface monolayers.

As previously discussed for Nb_3Cl_8 [24,28] and mentioned above and in Appendix A 10, these effective monolayers likely host variants of magnetic spin-spiral states. Thus, all stacks with at least one unpaired surface layer can be classified as magnetic, which potentially break TRS. In contrast, stacks consisting of fully dimerized bilayers have strongly suppressed magnetic properties as a result of the effective singlet formation, such that TRS likely stays intact.

However, whether a magnetic spin-spiral state and its potential TRS breaking also has a global effect on the electronic properties might depend on the electron coherence length [75]. If the latter is smaller than the spin-spiral wavelength, there might be a global effect. For example, the 120° Néel state of monolayer Nb_3Cl_8 seems to leave the TRS in tact after backfolding to the primitive unitcell intact [28]. We find the spin-spiral wavelengths to be ranging from 10 to 18.5 Å in Nb_3Cl_8 and Nb_3I_8, respectively (see Appendix A 10), which is on the same order as the electronic coherence length of other Mott insulators [76–78]. Based on this, we assume a possible global effect of the TRS breaking in the surface monolayers of Nb_3Br_8 and Nb_3I_8, but possibly not in $Nb_3F_8^*$ and Nb_3Cl_8. Additionally, we note that the interfaces to the superconducting leads in $NbSe_2/Nb_3Br_8/NbSe_2$, as well as magnetic impurities, might further contribute to the TRS breaking.

Taken together and as summarized in Fig. 13, this suggests that odd stacks of Nb_3Br_8 and Nb_3I_8 might intrinsically allow for the field-free Josephson diode effect, while Nb_3Cl_8 and $Nb_3F_8^*$ or in the case of fully dimerized bilayers in even stacks, interface effects to the encapsulating superconductors or impurities might be additionally required.

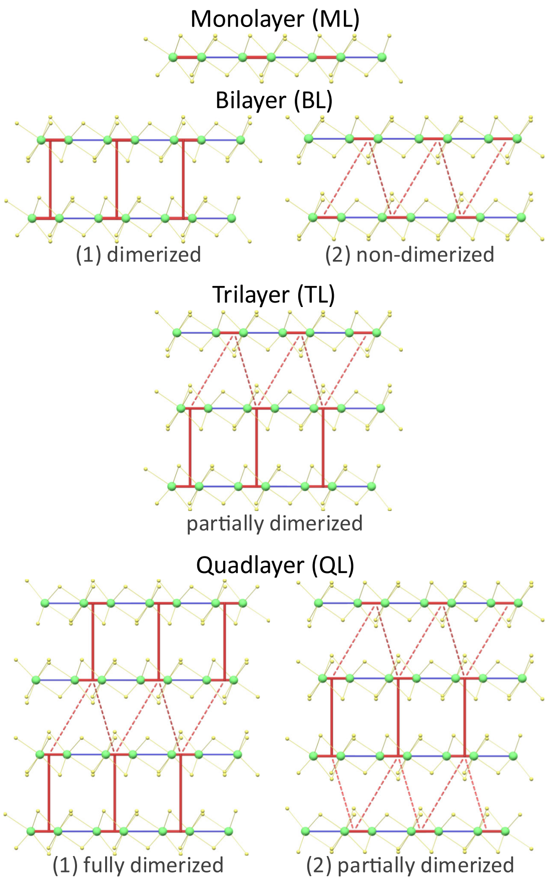

	Nb_3F_8*		Nb_3Cl_8		Nb_3Br_8		Nb_3I_8	
	IS	TRS	IS	TRS	IS	TRS	IS	TRS
ML	X	✓	X	✓	X	(X*)	X	(X*)
BL (1)	✓	✓	✓	✓	✓	✓	✓	✓
BL (2)	✓	✓	✓	✓	✓	(X*)	✓	(X*)
TL	X	✓	X	✓	X	(X*)	X	(X*)
QL (1)	✓	✓	✓	✓	✓	✓	✓	✓
QL (2)	✓	✓	✓	✓	✓	(X*)	✓	(X*)

FIG. 13. Symmetries of finite stacks of LT ($R\bar{3}m$) Nb_3X_8. Inversion and time-reversal symmetry in monolayer, bilayer, trilayer, and quadlayer of Nb_3X_8, taking into account various surface ("edge") terminations. The solid dark red line represents strong interlayer coupling between the nearest trimers, while the dashed line indicates weak coupling. Crosses (in brackets) indicate (possible but not necessary) symmetry breaking. Red check marks denote the preservation of symmetry.

III. CONCLUSION AND DISCUSSION

Our analysis shows that the low-energetic electronic structure as well as the magnetic properties of the whole class of Nb_3X_8 are dominated by the formation of flat bands as a result of the breathing-mode kagome distortion. Since the resulting low-energetic bands are well separated from those formed by all other Nb and halide orbitals, low energy generalized Hubbard models can be reliably obtained by *ab initio* downfolding using the constrained random phase approximation in combination with Wannier orbitals representing molecular orbitals centered at the trimerized Nb clusters.

The resulting models properly render the local chemistry of the effective molecular orbitals as well as the global screening properties. This allows us to quantify the strengths of in- and out-of-plane hopping as well as local and non-local Coulomb matrix elements in a material-specific manner. Our *ab initio* model database further shows that the whole material family is in the regime of strong local interaction ($U_0/t_\parallel > 60$). Since the ratios between these kinetic and local interaction terms vary from monolayer to bulk structures and from $Nb_3F_8^*$ to Nb_3I_8 as a result of modifications to the global screening, as well as from varying local confinements of the molecular orbitals, the degree of Coulomb correlations gradually decrease from $Nb_3F_8^*$ to Nb_3I_8 and from ML to bulk structures. Based on a strong coupling expansion we can further derive effective magnetic models, which show that the high-temperature crystal structures host interlayer magnetic frustrations, which are lifted by an effective singlet formation in the low-temperature structures. As these frustrations are the strongest in Nb_3I_8 and gradually diminish in Nb_3Br_8 and Nb_3Cl_8 accompanied by an decreasing energy gain from singlet formation, the accompanying critical temperatures of the crystallographic phase transition also gradually decrease from Nb_3I_8 to Nb_3Cl_8.

As a result, the low-temperature bulk materials are best understood as dimerized bilayers, which only couple weakly among each other through vdW interactions. The magnetic ground states are thus most likely singlets formed between interlayer neighboring spins localized on the strongly hybridized molecular orbitals. On the electronic side, our combined cRPA and cluster DMFT calculations show that the halide atoms control the ratios between the local Coulomb interactions and the in- and out-of-plane hopping terms and thereby drive the low-temperature bulk materials from a conventional two-band Mott insulator ($Nb_3F_8^*$) to strongly correlated insulators (Nb_3Cl_8 and Nb_3Br_8) and finally to a weakly correlated band insulator (Nb_3I_8). Moreover, since the screening is significantly reduced in the bilayer structures, we find that even the Nb_3I_8 bilayer becomes a strongly correlated insulator. In turn, due to the missing out-of-plane dimerization, all monolayer, as well as high-temperature structure variants of Nb_3X_8, are single- or two-band Mott insulators, respectively. Thus, already in the undoped case the class of Nb_3X_8 host several correlated ground states of different characters. To differentiate between these variants of strongly and weakly correlated insulators, we showed how the charge-neutral and temperature dependent excitations spectra as well as the charged excitation spectra of the local (interlayer molecular) dimer differ and how this is reflected in experimentally accessible dispersive bonding and nearly nondispersive antibonding lower Hubbard bands.

These correlated states can further be tuned either by doping or by the thickness of finite stacks. We showed that upon electron doping Nb_3X_8 can be driven through intermediate states of correlated metals to charge transfer or conventional Mott insulators. Furthermore, as a result of the alternating strong and weak hybridziation between adjacent layers, finite stacks of Nb_3X_8 can host weakly hybridized surface monolayers, which host on their own already at half-filling Mott insulating states.

In terms of the in-plane trimerization, similar compounds, such as Mo_3O_8, are also accompanied by strong correlations [79], but do not allow for single molecular orbital Hubbard model descriptions. In terms of the out-of-plane dimerization, Nb_3X_8 shares many similarities with bulk VO_2, one of the most well-studied correlated systems. It also hosts a crystal structure transition from a high temperature to a low temperature phase, which is accompanied by a dimerization of the vanadium atoms into pairs resulting in singlet formation [80,81]. The latter yields a correlated gapped state, which is driven by strong Coulomb correlation effects, the dimerization, and the accompanying singlet formation [82–85], which can also be understood using a molecular orbital bonding and antibonding Wannier basis [86,87]. However, the vdW material class of Nb_3X_8 comes with the significant advantage of a rather simple low-energy band structure, which allows for a clean disentanglement and thus for a trustworthy downfolding to minimal correlated models.

Thus, the combination of in-plane trimerization and out-of-plane dimerization renders Nb_3X_8 an extremely robust, versatile, but also simple platform to study and engineer many-body phenomena. In combination with the various and tunable degree of correlations, Nb_3X_8 can thus be seen as a promising *drosophila melanogaster* of layered correlated (Mott) insulators, which offers the exciting possibility to precisely study numerous correlation phenomena both theoretically and experimentally. The models which we derived here yield an optimal theoretical framework for this purpose, and the complete model specifications for the entire Nb_3X_8 family are made freely available via a public repository, see Ref. [88].

IV. OUTLOOK

An important difference to other prototypical bulk strongly correlated insulators is that as a result of the layered vdW structure screening is generically suppressed in Nb_3X_8, such that significantly long-ranged Coulomb interactions are present, cf. Table I. These could yield a nonlocal coupling of holons and doublons forming

Mott excitons [89] in the strongly correlated insulators Nb_3Br_8 and Nb_3Cl_8 or conventional excitons in Nb_3I_8, which could be influenced by the magnetic properties of the system. We can thus expect in-gap features in optical spectroscopy experiments, which might have been experimentally seen already in the case of Nb_3Cl_8 [23,45]. Furthermore, in few- or monolayer systems, these nonlocal Coulomb interactions are tunable by means of environmental screening as, e.g., resulting from substrate materials. Together with first indications that long-range Coulomb interactions in combination with doping could yield novel charge ice states [42], this renders Nb_3X_8 a promising platform for strong-correlation engineering of unconventional magnetic, charge, or superconducting order but also of optical effects via nonlocal Coulomb interactions [90].

Another intriguing many-body engineering pathway is via chemical modification, such as already realized in admixtures of the form $Nb_3X_{8-x}Y_x$ with X and Y being both halide atoms [23,39]. As the halide controls the degree of correlation in this system class, such admixtures might be best understood as disordered (strongly) correlated (Mott or charge transfer) insulators. Alternatively, $Nb_3X_{8-x}Y_x$ with Y being a chalcogen atom [65,66] might allow for precise chemical doping to access the predicted strongly correlated metal regime and to realize the recently suggested Sordi transition [91].

Finally, the vdW nature of Nb_3X_8 offers the possibility to mix and stack them into layered vdW heterostructures. Experimentally, this has already been done in the form of $NbSe_2/Nb_3Br_8/NbSe_2$ heterostructures, which host nonreciprocal superconducting properties. Taking furthermore into account the different degrees of correlations already present within the class of Nb_3X_8, stacking them into $Nb_3X_8/Nb_3Y_8/Nb_3Z_8$ heterostructures and/or mixing them with other correlated layered materials opens up an incredibly rich new toolbox for designing strongly correlated vdW heterostructures, e.g., with spatially varying local Coulomb interaction strengths. So far, there is only 4Hb-TaS_2, which comes with similar possibilities [92,93]. The electronic structure of 4Hb-TaS_2 is, however, drastically more involved, requiring additional approximations, which are not necessary within the class of Nb_3X_8. This allows, e.g., for implementing the proposal of enhanced critical temperatures in superconducting heterostructures [94] or to realize Mott field effect transistors or correlated Schottky barriers.

Taking all these chemically, environmentally, and/or doping tunable correlation phenomena in Nb_3X_8 into account renders this material class an exciting framework for many-body functionalization concepts. For these and other functionalization schemes, we however stress that the interfaces to other (substrate) materials as well as among different variants of Nb_3X_8 need to be studied in detail.

V. METHODS

A. *Ab initio* modeling

1. *Density functional theory calculations and lattice structure relaxations*

We investigate the material-specific electronic structure starting from DFT calculations using the Perdew-Burke-Ernzerhof GGA exchange-correlation functional [95] within a basis of projector augmented waves [96] as implemented in the Vienna *ab initio* simulation package (VASP) [97,98]. We apply a Gaussian smearing of 0.05 eV and a plane-wave cutoffs of 550 eV for $Nb_3F_8^*$ and Nb_3Cl_8 and 350 eV for Nb_3Br_8 and Nb_3I_8 and use pseudopotentials from VASP 6.4. Van der Waals corrections were added according to DFT-3 method of Grimme. The electronic self-consistency criterion was set to 10^{-7} eV and the k points were sampled on $6 \times 6 \times 6$ k grids.

We conducted lattice and structural optimizations for all compounds in their LT (also for Nb_3Cl_8 and Nb_3Br_8 in HT) bulk phases, keeping the space group fixed at $R\bar{3}m$ (at $P\bar{3}m1$). Atomic positions were allowed to relax until the forces on each atom fell below 0.01 eVÅ^{-1}. Mono- and bilayer structures were derived from the relaxed bulk phases by introducing a vacuum space that is 3 times larger than the interlayer spacing between the nearest Nb layers. The details of the relaxed lattice parameters are summarized in Tables I and IV. Additionally, all atomic positions and calculation inputs are accessible through our public repository [88].

TABLE IV. Structural and *ab initio* downfolded many-body Hamiltonian parameters for HT ($P\bar{3}m1$) Nb_3Cl_8 and Nb_3Br_8. In-plane (a) and out-of-plane (c) lattice parameters, molecular orbital spread (Ω), nearest neighbor in-plane ($t_\parallel$) and out-of-plane ($t_\perp$) hopping parameters and corresponding cRPA screened Coulomb ($U_\parallel$ and $U_\perp$) interactions, on-site bare (V_0) and screened (U_0) Coulomb interactions including their ratio $\epsilon_{\text{eff}} = V_0/U_0$. t, U and V are provided in meV.

	Nb_3Cl_8	Nb_3Br_8
a (Å)	5.84	6.14
c (Å)	12.28	12.94
d_2/d_1	1.40	1.47
Ω (Å^2)	7.26	8.69
$t_\parallel$	23.54	10.69
$t_\perp^{(s)}$	−17.11	−20.56
$t_\perp^{(w)}$	−15.92	−20.25
V_0	6088.7	5752.7
U_0	1401.0	1129.1
ϵ_{eff}	4.35	5.09
$U_\parallel$	460.0	360.2
$U_\perp^{(s)}$	336.8	276.5
$U_\perp^{(w)}$	299.2	242.0

2. Wannier function basis, constrained random phase approximation calculations, and many-body model matrix elements

Following the recipe from Ref. [24] and starting from the DFT calculations described above, we use WANNIER90 [99] to construct molecular orbitals describing the two low energy bands of our DFT calculation. To this end we start from s-orbital projections localized at the centers of the small trimers and proceed with a maximal localization of the Wannier functions.

Within this basis, we calculate all single-particle (hopping) and many-body (Coulomb) matrix elements according to $t_{ij} = \langle\psi_i|\hat{H}_{\mathrm{DFT}}|\psi_j\rangle$ and $U_{ijkl} = \langle\psi_i\psi_j|\hat{U}_{\mathrm{cRPA}}(\omega=0)|\psi_k\psi_l\rangle$, respectively. For the latter we use the constrained random phase approximation (cRPA) as implemented in VASP [100]. To converge the bare Coulomb matrix elements as well as the cRPA polarization we vary the plane-wave cutoffs as well as the number of involved bands until changes are smaller than ca. 50 meV in the cRPA screened local Coulomb interaction U_0. This requires Coulomb matrix element cut-offs between 350 and 550 eV and up to 256 bands. For the extraction of monolayer and bilayer Coulomb matrix elements, we further apply an extrapolations scheme as described in Appendix A 1. Since the electronic gaps in the "rest" band structures are rather large and since the low-energy flat bands are not entangled with the rest space, using the static limit of the cRPA screening is a good approximation for the $\mathrm{Nb_3X_8}$ material class [24].

In Tables I and IV we show the most relevant matrix elements for the discussion of the LT and HT compounds, respectively. All other elements, including all necessary parameter files, are available via our $\mathrm{Nb_3X_8}$ model parameter database [88].

3. DMFT

The resulting generalized Hubbard models are solved using dynamical mean-field theory using TRIQS [101], applying two different impurity solvers. At integer filling and large U/t, the Hubbard-I approximation provides a good description of the physics while being computationally efficient and giving access to real-frequency data directly. We use the implementation by Schüler [102]. The Hubbard-I spectral functions in Figs. 8, 10, 17, and 21 are calculated at $\beta = 5000\ \mathrm{eV}^{-1}$ for $\mathrm{Nb_3F_8^*}$, $1000\ \mathrm{eV}^{-1}$ for $\mathrm{Nb_3Cl_8}$, and $100\ \mathrm{eV}^{-1}$ for $\mathrm{Nb_3Br_8}$ and $\mathrm{Nb_3I_8}$. This ensures that the contribution to the spectrum from the first excited state, which is less and less separated in energy from $\mathrm{Nb_3I_8}$ to $\mathrm{Nb_3F_8^*}$, is sufficiently small. The results are (Lorentzian) broadened with $\delta = 0.01$ eV.

For the doped system, we use the continuous-time hybridization expansion [103–106] (CTHYB) solver implemented in w2dynamics [107] with worm sampling [108,109]. The discrete Lehmann representation [110–112] is used to represent the Green's functions efficiently. The DMFT calculations were carried out at $\beta = 100\ \mathrm{eV}^{-1}$.

We track the electron density $N = \mathrm{Tr}(\hat{\rho})$, with $\hat{\rho} = G(\tau = 0^-)$, upon changes in the chemical potential. To facilitate the analysis, the self-energy and related quantities are shown in the bonding and antibonding basis which nearly diagonalizes the self-energy and dispersion (off-diagonal components are at least 2 orders of magnitude smaller than diagonal). The approximate quasiparticle weight is then derived from the self-energy on the Matsubara axis

$$Z = \left(1 - \left.\frac{\mathrm{Im}\,[\Sigma(i\omega_n)]}{\omega_n}\right|_{\omega_n\to 0}\right)^{-1}, \qquad (3)$$

as discussed in Ref. [113].

The Matsubara self-energies are analytically continued using the minimal pole representation method recently introduced by Zhang *et al.* [67,68], whereby all poles were restricted to lie on the real axis. Consequently, the relative strength and energy of excitations are captured, but broadening effects due to interaction are disregarded.

B. Phonon calculations

All DFPT calculations are performed within QUANTUM ESPRESSO [114,115] v7.3.1 and cDFPT calculations within v7.4.1 using v1.2 norm-conserving pseudopotentials from the Schlipf-Gygi library [116] as available via http://www.quantum-simulation.org. For the cDFPT calculations we used the patch provided by Berges via the elphmod package [117]. All structures are re-relaxed with respect to the atomic positions using the lattice vectors from our VASP relaxations (as described above in section V A), $6 \times 6 \times 6$ k meshes, energy cut offs of 100 and 400 Ry for the wave functions and charge density, respectively, and a force convergence threshold of 10^{-6} Ry/Bohr. (c)DFPT calculations are subsequently performed on $2 \times 2 \times 2$ q meshes. If not stated otherwise, we applied acoustic sum rules.

The raw data as well as all necessary parameter files are available via our $\mathrm{Nb_3X_8}$ model parameter database [88].

C. Effective exchange interaction parameters

Given the on-site Coulomb interactions are significantly larger than the hopping matrix elements in all $\mathrm{Nb_3X_8}$ compounds (see Tables I and IV), we apply a strong-coupling expansion to obtain exchange interactions of the form

$$J_{\perp/\parallel} = -2(t_{\perp/\parallel})^2/U^{\mathrm{eff}}_{\perp/\parallel},$$

where labels $\perp$ and $\parallel$ denote sites i and j in the out-of-plane and in-plane directions, respectively. Instead of using U_0 in the equation above, we employ $U^{\mathrm{eff}}_{\perp} = U_0 - U^{(s)}_{\perp}$ and $U^{\mathrm{eff}}_{\parallel} = U_0 - U^{(1)}_{\parallel}$ for the out-of-plane and in-plane values, respectively. This includes the renormalization of the energy cost due to nonlocal Coulomb interactions [24] and can be understood as the renormalization of the energy cost associated with virtual doublon-holon excitations due to nonlocal Coulomb interactions [56]. Such renormalization is essential for accurately capturing charge-neutral excitations; however, it is not suitable for spectral functions, which describe excitations involving changes in total charge [24,118]. The resulting exchange interactions for both Nb_3X_8 monolayers and Nb_3X_8 bulk are presented in Tables II and III, respectively.

D. Atomistic spin dynamics simulations

To investigate the ground-state magnetic properties of the surface Nb_3X_8 monolayers, as well as the temperature and magnetic field dependence of the magnetic susceptibility in bulk Nb_3Cl_8, we utilize spin dynamics simulations conducted with the SPIRIT code [119]. All simulations are based on a classical Heisenberg Hamiltonian given by Eq. (2). Our simulations are grounded in the Landau-Lifshitz-Gilbert (LLG) equation of motion to assess ground-state properties, while we employ classical Monte Carlo (MC) calculations to compute the magnetic susceptibility. Our test simulations indicate that a lattice of $50 \times 50 \times 1$ spins is sufficient for the surface monolayer simulations (solving the LLG equations), while a $20 \times 20 \times 4$ spins suffices for the bulk simulations (using the MC method). To minimize boundary effects, for the surface monolayer case, we consider only in-plane periodic boundary conditions, whereas for the bulk case, periodic boundaries are applied in all dimensions.

In the Monte Carlo simulations, we employed 500 thermalization steps, followed by 1 000 000 samples in the Metropolis algorithm, and conducted five decorrelation steps. The isothermal susceptibility is evaluated according to

$$\chi = \frac{1}{k_B T}(\langle \mathbf{M}^2 \rangle - \langle \mathbf{M} \rangle^2),$$

where $\mathbf{M} = (1/N)\sum_i^N \mathbf{S}_i$ represents the average magnetization of the sample.

E. ARPES measurements

Nb_3Br_8 and Nb_3I_8 crystals were synthesized using chemical vapor transport [30]. To avoid air exposure, crystals were mounted in a glove box and transferred to the beamline in a vacuum suitcase. Samples were cleaved *in situ* prior to ARPES measurements. The ARPES measurements were performed at the SGM3 beamline of the ASTRID2 synchrotron radiation facility at Aarhus University in Denmark [120]. Measurements were carried out at 150 K with a base pressure of 1×10^{-10} mbar. The ARPES data were acquired at photon energies ($h\nu$) ranging from 30.5 to 130.5 eV, with energy and angular resolutions better than 50 meV and 0.2°, respectively. The beam spot size was 190 μm × 90 μm. The synchrotron radiation polarization and the sample-to-analyzer direction were both in the plane of incidence, and the analyzer slit was perpendicular to the plane of incidence. The EDC fitting used a linear background and Voigt profiles, employing the minimum number of fitting components required for accurate fits.

ACKNOWLEDGMENTS

The authors acknowledge useful discussions with Alberto Carta, Claude Ederer, Dmytro Afanasiev, Dieter Vollhardt, Giorgio Sangiovanni, Mikhail Titov, Maurits Haverkort, Roser Valentí, Antoine Georges, Andrew J. Millis, and Silke Biermann. The authors especially thank Emanuel Gull and Lei Zhang for supporting the analytical continuation using Prony as well as Jan Berges for helpful discussions on the phonon calculations. We acknowledge the National Academic Infrastructure for Supercomputing in Sweden (NAISS), partially funded by the Swedish Research Council through Grant Agreement No. 2022-06725, for awarding this project access to the LUMI supercomputer, owned by the EuroHPC Joint Undertaking and hosted by CSC IT Center for Science (Finland) and the LUMI consortium, as well as computer resources hosted by the PDC Center for High Performance Computing and the National Supercomputer Centre (Projects No. NAISS 2023/1-44, No. 2023/6-129, No. 2023/8-9, No. 2024/1-18, No. 2024/6-127, and No. 2024/8-15) where the computational pipeline was developed and tested. The material specific computations were performed at the Dutch National Supercomputer Snellius under Projects No. EINF-11321 and EINF-7490. X. L. acknowledges Guangzhou Elite Project scholarship (S. J. [2022] No. 1). Z. D. acknowledges the fellowship from the Chinese Scholarship Council (No. 202206750016). M. W. acknowledges financial support from the Punjab Educational Endowment Fund (PEEF). A. G. C. acknowledges the financial support of the Zernike Institute for Advanced Materials. P. H. acknowledges support from the Independent Research Fund Denmark (Grants No. 4258-00002B and No. 1026-00089B). M. I. K. and H. U. R. S. acknowledge funding from the European Research Council (ERC) under the European Union's Horizon 2020 research and innovation programme (Grant Agreement No. 854843-FASTCORR). EGCPvL acknowledges support from the Swedish Research Council (Vetenskapsrådet, VR) under Grant No. 2022-03090, from the Royal Physiographic Society in Lund and by eSSENCE, a strategic research area for e-Science, Grant No. eSSENCE@LU 9:1. M. I. K. and M. R. acknowledge support from the Dutch Research Council (NWO) via the "TOPCORE" consortium. J. A., C. K., M. W., M. A., M. I. K., A. G. C., and M. R. acknowledge support from the research program "Materials for the Quantum Age" (QuMat). This program (registration No. 024.005.006) is part of the Gravitation program financed by the Dutch Ministry of Education, Culture and Science (OCW). M. R. acknowledges support from the Vidi ENW research programme of the Dutch Research Council (NWO) [Grant DOI: 10.61686/YDRHT18202] with file number VI.Vidi.233.077.

DATA AVAILABILITY

The data that support the findings of this article are openly available [88].

APPENDIX

1. Vacuum extrapolation of the mono- and bilayer cRPA Coulomb matrix elements

For the mono- and bilayer cRPA calculations we separate the mono- or bilayers by an effective vacuum of 3 times their individual monolayer heights. Since the true freestanding limit would only be achieved by further increasing this effective "vacuum height" these cRPA calculation suffer from spurious screening from the periodic replicas of the systems in the c direction. To extrapolate the Coulomb matrix elements to the true freestanding limit, we make use of our Wannier function continuum electrostatic (WFCE) approach [121] as applied for monolayer $\mathrm{Nb_3Cl_8}$ in Ref. [24].

To this end, we start with the nonlocal bare Coulomb interaction of the mono- and bilayer as obtained from our cRPA calculations in momentum space. Within a matrix representation $v_{\alpha\beta}(q)$ using a product basis $\alpha, \beta = \{n, m\}$ we can diagonalize the Coulomb tensor $v(q) = \sum_\nu v_\nu(q)|v_\nu(q)\rangle\langle v_\nu(q)|$ with $v_\nu(q)$ and $|v_\nu(q)\rangle$ being the corresponding eigenvalues and eigenvectors of the Coulomb tensors and $q = |\mathbf{q}|$. Assuming that the eigenbasis does not drastically change upon the effects of the cRPA screening, we can thus represent the full cRPA Coulomb tensor as $U(q) = \sum_\nu \{[v_\nu(q)]/[\varepsilon_\nu(q)]\}|v_\nu(q)\rangle\langle v_\nu(q)|$, where $\varepsilon_\nu(q)$ are the corresponding pseudoeigenvalues of the dielectric tensor describing the different screening channels. The leading eigenvalue $v_1(q)$ renders Coulomb penalties for monopolelike perturbations (all orbitally resolved electronic densities are in phase). The monopolelike screening as rendered by $\varepsilon_1(q)$ can be modeled by solving the Poisson equation for a dielectric slab of height h embedded in some different dielectric environment yielding

$$\varepsilon_1(q) = \frac{\varepsilon_1^{(0)}\left[1 - \tilde{\varepsilon}_0^{(1)}\tilde{\varepsilon}_0^{(2)}e^{-2qh}\right]}{1 + \left[\tilde{\varepsilon}_0^{(1)} + \tilde{\varepsilon}_0^{(2)}\right]e^{-qh} + \tilde{\varepsilon}_0^{(1)}\tilde{\varepsilon}_0^{(2)}e^{-2qh}} \quad \text{with}$$

$$\tilde{\varepsilon}_0^{(1)} = \frac{\varepsilon_1^{(0)} - \varepsilon_{\mathrm{sub}}^{\mathrm{below}}}{\varepsilon_1^{(0)} + \varepsilon_{\mathrm{sub}}^{\mathrm{below}}}, \qquad \tilde{\varepsilon}_0^{(2)} = \frac{\varepsilon_1^{(0)} - \varepsilon_{\mathrm{sub}}^{\mathrm{above}}}{\varepsilon_1^{(0)} + \varepsilon_{\mathrm{sub}}^{\mathrm{above}}}. \tag{A1}$$

Example results for $\varepsilon_1(q)$ of the inital cRPA calculations for mono- and bilayer $\mathrm{Nb_3F_8^*}$ are shown in Fig. 14. For both structures we see that $\varepsilon_{q=0} > 1$ which is indicative for the spurious interlayer screening due to the finite effective vacuum height. However, we also find that we can fit the raw initial cRPA data with the analytic $\varepsilon_1(q)$ function from above well, finding $\varepsilon_{\mathrm{sub}}^{\mathrm{above}} = \varepsilon_{\mathrm{sub}}^{\mathrm{below}} > 1$ (blue curves in Fig. 14). By setting $\varepsilon_{\mathrm{sub}}^{\mathrm{above}} = \varepsilon_{\mathrm{sub}}^{\mathrm{below}} = 1$ we enforce $\varepsilon_{q=0} = 1$ (orange curves in Fig. 14). This way we correct for the artificial spurious inter-layer screening. Using this corrected ε_q and the bare v_q we can reconstruct the vacuum corrected U_q from which we calculate in a final step via Fourier transforms the real space U_R, which are listed in Table I.

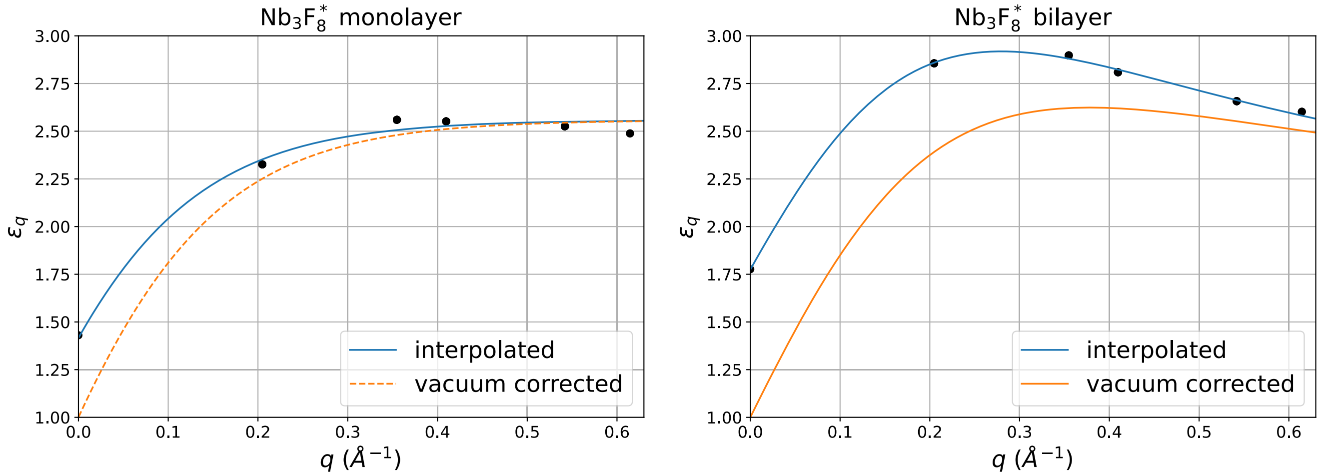

FIG. 14. Leading cRPA dielectric functions of monolayer (left) and bilayer (right) $\mathrm{Nb_3F_8^*}$. Markers indicate initial *ab initio* calculation results. Blue lines are analytic fits to the *ab initio* data. Orange lines represent the "vacuum corrected" behavior. For the monolayer $\varepsilon_1^{(0)}$ was assumed to be a constant, while we used a Resta-like q-dependent model for the bilayer.

2. Exact diagonalization of the dimer model and relevance of Hedin vertices

In order to establish the notion of strong and weak correlations we perform calculations using strong (Hubbard-I) and weak coupling (Hedin's GW) approximations. Comparing the results enables us to classify the compounds in the $\mathrm{Nb_3X_8}$ family with respect to the degree of correlation effects.

We start this analysis by investigating the local (impurity) Green's functions in more detail. In the Hubbard-I approximation these are equivalent to the exact diagonalization (ED) results of a generalized Hubbard dimer using the full U_{ijkl} tensor and an effective dimerization $\tilde{t}_\perp$, where i, j, k, l belong to one of the two sites representing the two molecular orbitals of the strongly hybridized or dimerized planes.

For the (simplified) Hubbard dimer with only local Coulomb interactions (i.e., only $U_{iiii} = U$ terms taken into account), the exact interacting Green's functions and the G_0W_0 approximation can both be derived analytically [22,122]. The latter neglects all (Hedin) vertex contributions. The corresponding self-energies read

$$\Sigma_{\mathrm{ED}}(\nu) = \frac{U^2}{4}\frac{1}{\nu \mp 3\tilde{t}_\perp}, \tag{A2}$$

$$\Sigma_{G_0W_0}(\nu) = \frac{U^2\tilde{t}_\perp}{c}\frac{1}{\nu \pm \tilde{t}_\perp \pm c}, \tag{A3}$$

with $c = \sqrt{4\tilde{t}_\perp^2 + 4U\tilde{t}_\perp}$. To connect this simple model to our ED calculations with the full U_{ijkl}, we fit the self-energy of the latter using the effective dimerization $\tilde{t}_\perp$ as the fit parameter. We find $\tilde{t}_\perp \approx 0.00$, 0.15, 0.19, and 0.25 eV for F, Cl, Br, and I, respectively. Setting U to the cRPA downfolded values U_{iiii}, the analytic self-energies of the simplified Hubbard dimer fit the full ED ones very well. By further comparing the Hubbard-I spectral functions obtained with and without the nonlocal Coulomb interactions between the two molecular orbitals of the dimer (see Appendix A 4), we find the that nonlocal Coulomb interactions do not affect the single particle Green's functions at half filling.

We therefore compare in Fig. 15 the spectral functions of $G_{\mathrm{ED}}(\omega)$ and $G_{G_0W_0}(\omega)$ obtained for the simplified Hubbard dimer allowing us to study how relevant Hedin vertex corrections are for each system. In the case of $\mathrm{Nb_3Cl_8}$ we see that the ED and G_0W_0 show significant discrepancies. In detail, the ED result shows a gapped local spectral function with two main peaks forming the gap, which are accompanied by two side peaks with reduced spectral weight. We can understand these four features as lower and upper Hubbard bands from the bonding and antibonding orbitals, whereby the gap is formed between the lower Hubbard band of the bonding orbital and the upper Hubbard band of the antibonding orbital. In the G_0W_0 approximation, we find a similar pole structure. However, the inner poles are at much smaller energies, while the outer poles are at much higher energies with suppressed spectral weight. Also, the nature of the G_0W_0 approximation does not allow us to identify the different poles as resulting from Hubbard bands. Instead, in the G_0W_0 approximation a more appropriate interpretation would be as shake-off bands resulting from charge fluctuations. Altogether, this clearly stresses the relevance of Hedin vertices for a qualitatively and quantitatively correct description of $\mathrm{Nb_3Cl_8}$. This allows us to identify $\mathrm{Nb_3Cl_8}$ as a strongly correlated insulator. The same holds for $\mathrm{Nb_3Br_8}$, albeit with smaller deviations between ED and G_0W_0 results. $\mathrm{Nb_3F_8^*}$ in turn starts from a metallic regime and is neither quantitatively nor qualitatively well described within the G_0W_0 approximation. The ED gap of $\mathrm{Nb_3F_8^*}$ can thus be best understood as a conventional Mott gap opened by a self-energy of the form $U^2/(4\nu)$. Finally, for $\mathrm{Nb_3I_8}$ we see that the two results are qualitatively and quantitatively very similar such that we can understand $\mathrm{Nb_3I_8}$ as a weakly correlated insulator, which is well approximated by the G_0W_0 scheme.

3. Single-site vs cluster dynamical mean field theory

In Fig. 16 we show the differences between a cluster and a single-site DMFT calculation, which, respectively,

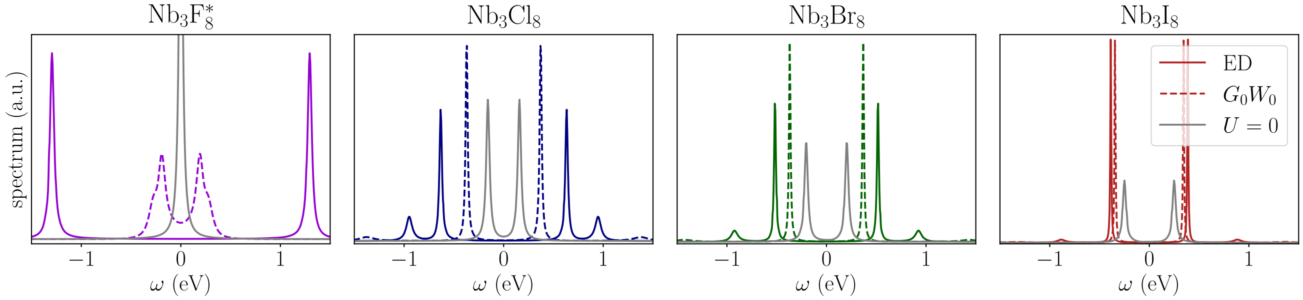

FIG. 15. Dimer model results using parameters from cRPA. We compare bare bonding-antibonding splitting (gray solid line) with dimer G_0W_0 results (dashed lines) and exact diagonalization results (colored solid lines).

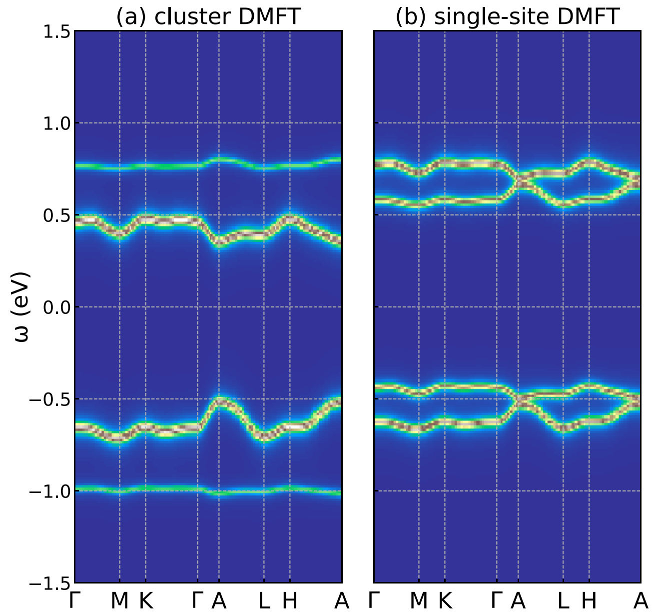

FIG. 16. Bulk LT ($R\bar{3}m$) Nb_3Br_8 in a cluster and single-site Hubbard-I calculation.

include the full matrix structure of the self-energy or just its diagonal components in the molecular orbital basis, for the low-temperature bulk structure of Nb_3Br_8. From this it is clear that to correctly describe the bonding and antibonding Hubbard bands, cluster DMFT in a full two-molecular-orbital basis is necessary.

4. Hubbard-I spectral functions with only on-site Coulomb interaction

In Fig. 17 we show the Hubbard-I spectral functions for $N_e = 2$ and $N_e = 3$ obtained using only local Coulomb interactions (U_{iiii}). Comparing these to Fig. 8 and Fig. 10, respectively, allows us to investigate the role of the interlayer dimer density-density Coulomb matrix elements (between the molecular orbitals ψ_1 and ψ_2) as all other elements of the full U_{ijkl} tensor were already vanishingly small.

For the undoped case ($N_e = 2$), we find that the spectral functions do not change and the fundamental gaps are unaffected. This is different in the doped case ($N_e = 3$). Here, removing the interlayer dimer density-density

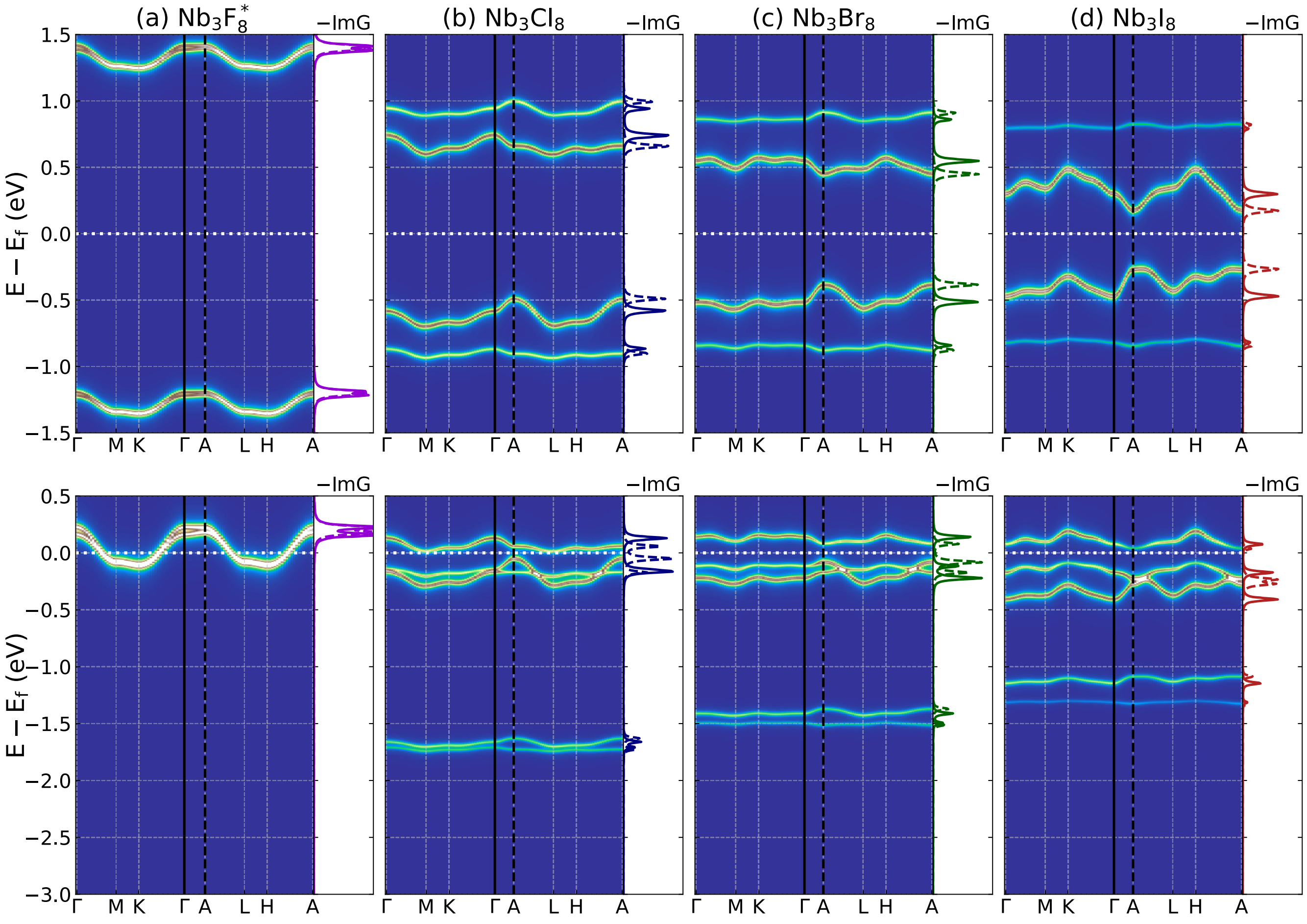

FIG. 17. (a)–(d) LT ($R\bar{3}m$) Nb_3X_8 cluster DMFT spectral functions within Hubbard-I with only on-site Coulomb interactions U_0 (but intercluster hybridization). For $N_e = 2$ (top row) and $N_e = 3$ (bottom row). Line cuts at Γ and A are shown in full and dashed lines, respectively.

Coulomb interaction changes the spectral functions quantitatively in the case of Cl, Br, and I, and even qualitatively in the case of F. In the former cases, all gaps between sets of bands are modified when we neglect nonlocal Coulomb interactions. However, the qualitative properties are the same. $\mathrm{Nb_3Cl_8}$ and $\mathrm{Nb_3Br_8}$ are still charge-transfer insulators and $\mathrm{Nb_3I_8}$ is still a (nearly) conventional Mott insulator. In the case of $\mathrm{Nb_3F_8^*}$ we, however, find a metallic solution as soon as we neglect the nonlocal Coulomb interaction at $N_e = 3$. The $\mathrm{Nb_3F_8^*}$ result at three quarter filling with only on-site Coulomb interaction should be taken with care. As there is no actual dimerization in this system on might interpret it as two separate Mott insulators at noninteger filling and thus possibly away from the regime in which the Hubbard-I approximation is applicable.

5. Full phonon dispersions

In Fig. 18 we show the full phonon dispersion for all four compounds in their LT bulk, bilayer, and monolayer structures as calculated within DFPT.

6. Constrained density functional perturbation theory calculations for $\mathrm{Nb_3F_8^*}$ and $\mathrm{Nb_3Cl_8}$

Within the cDFPT calculations we removed the two lowest bands around the Fermi level from the Sternheimer equation. For detailed comparison between the DFPT and cDFPT results, we show in Fig. 19 the phonon energies of LT bulk $\mathrm{Nb_3F_8^*}$ and $\mathrm{Nb_3Cl_8}$ at the original (coarse) q points without including any LO-TO splitting or applying any sum rules. The latter results in slightly imaginary frequencies at Γ (indicated as negative values). This comparison shows that the DFPT and cDFPT results are very similar with only a few (mostly higher energy) modes being affected. As expected, those modes which change in cDFPT are shifted to higher energies, since the energy cost of atomic displacements is higher when (some) electronic states cannot move along [123]. Overall, cDFPT effects are small in $\mathrm{Nb_3Cl_8}$ and only mildly larger in $\mathrm{Nb_3F_8^*}$. The electron-phonon coupling to the slightly gaped low-energetic flat bands of $\mathrm{Nb_3Cl_8}$ has thus a smaller effects to the phonons than the electron-phonon coupling to the metallic flat bands in $\mathrm{Nb_3F_8^*}$.

7. Doping dependence of DMFT Matsubara self-energies

Figure 11 shows the doping dependence of the approximate quasiparticle weights Z, which is calculated using Eq. (3) from the imaginary part of the Matsubara self-energy shown in Fig. 20. This self-energy is calculated in cluster DMFT using W2DYNAMICS.

At small doping the bonding components of the $\mathrm{Nb_3Cl_8}$ and $\mathrm{Nb_3Br_8}$ self-energies have a significant frequency dependence around zero frequency, which results in the nearly vanishing quasiparticle weight shown in Fig. 11(a). In contrast, for $\mathrm{Nb_3I_8}$ these retardation effects are strongly suppressed, resulting in a significant quasiparticle weight for $\mathrm{Nb_3I_8}$ at small doping. This is in line with our identifications as strongly ($\mathrm{Nb_3Cl_8}$ and $\mathrm{Nb_3Br_8}$) and weakly ($\mathrm{Nb_3I_8}$) correlated insulators at half-filling.

As the doping level increases towards $N_e = 3$ we see that the frequency response of the bonding component of the self-energies is suppressed in all compounds. As a consequence, the bonding channel becomes more and more coherent with doping. In the antibonding component we observe a qualitatively similar behavior, i.e., $\mathrm{Nb_3Cl_8}$ shows the strongest retardation effects and $\mathrm{Nb_3I_8}$ the weakest. With increasing doping these retardation effects increase for all compounds. Thus, under (strong) electron doping even $\mathrm{Nb_3I_8}$ shows correlation effects in the antibonding channel. In fact, close to $N_e = 3$ all systems seem to behave as hole-doped Mott insulators, which is reflected in the suppressed quasiparticle weights shown in Fig. 11(a).

8. Graphical solution of the dimer models

To further clarify and visualize the qualitative differences between the strongly and weakly correlated states (with and without doping), we present in Fig. 21 the graphical solutions of the Dyson equations governing the properties (local spectral functions) of the dimer models for all four compounds and for $N_e = 2$ and $N_e = 3$, respectively. In detail, we show for all cases $\mathrm{Re}\Sigma(\omega)$ and $\omega - \epsilon_{\mathrm{loc}}$ for both bonding and antibonding channels, with $\epsilon_{\mathrm{loc}} = \sum_{\mathrm{BZ}} \epsilon_k$. Therefore, the solutions to the equation

$$\omega - \epsilon_{\mathrm{loc}} = \mathrm{Re}[\Sigma(\omega)] \tag{A4}$$

define excitation energies (poles in the spectral functions).

For $N_e = 2$ we see in the left column of Fig. 21 three qualitatively different solutions. For $\mathrm{Nb_3F_8^*}$ we find (nearly) degenerate bonding and antibonding self-energies, both of which have a strong pole around $\omega = 0$. As a consequence of this (effectively) single-pole structure, we find two solutions to Eq. (A4) (around -1.2 and $+1.2$ eV) yielding two features in the spectral function. This is the classic Mott-gap scenario resulting in a lower and upper Hubbard band with a gap defined by the local Coulomb interaction strength U. In contrast, for the other compounds, we see that the bonding and antibonding self-energies still exhibit single poles, which are, however, shifted with respect to each other. As as result we find in all cases four distinct solutions, with two main spectral features around the gap and two accompanying side features. Upon close inspection we see that the upmost occupied state is given by a solution resulting from the bonding channel, and the lowest unoccupied one by a solution resulting from the antibonding channel. The fundamental gap is thus always opened between the bonding and antiboding channel. However, due to the large U in the case

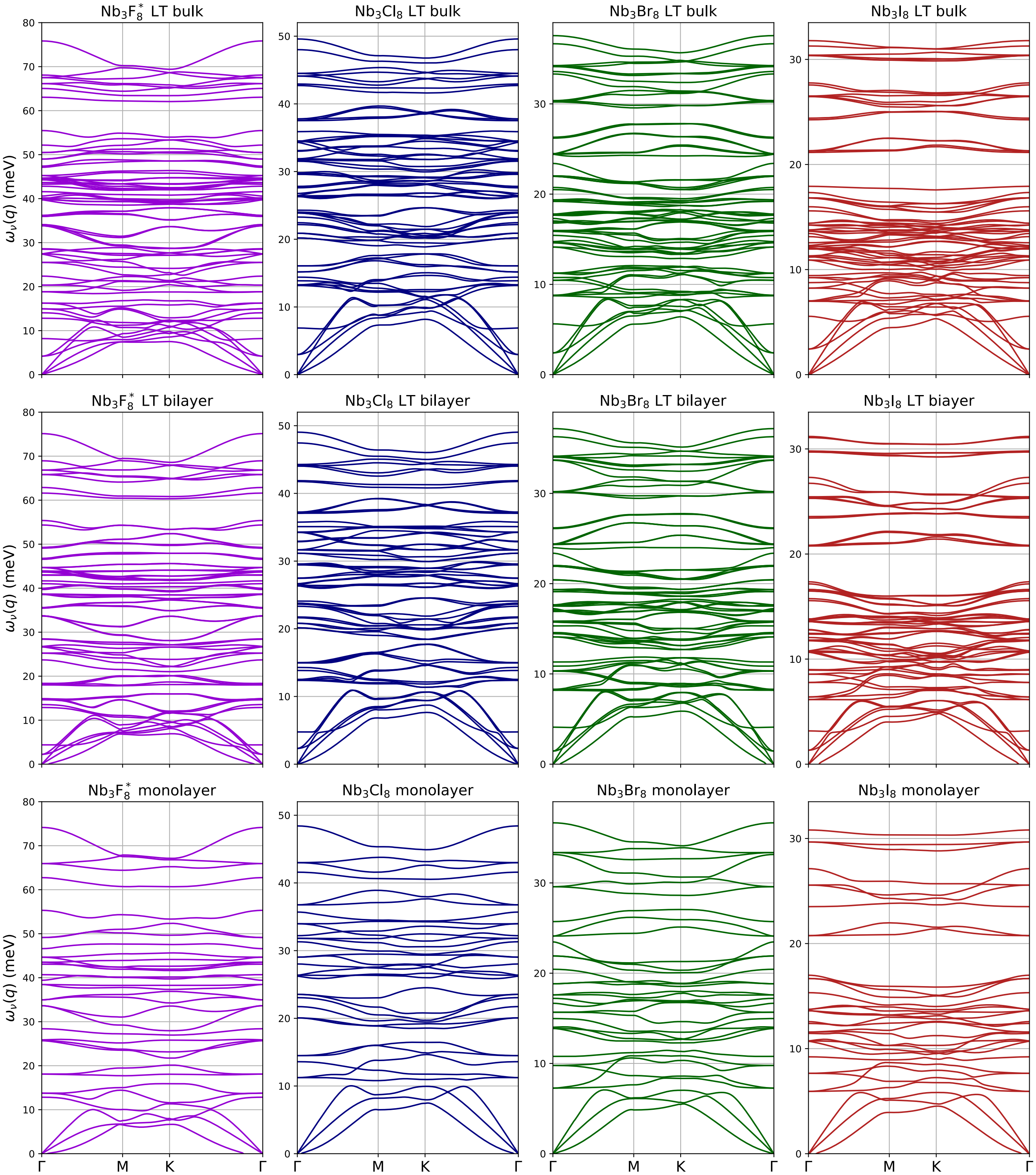

FIG. 18. DFPT phonon dispersions for $\mathrm{Nb_3X_8}$ in their LT ($R\bar{3}m$) bulk, bilayer, and monolayer structures.

of $\mathrm{Nb_3Cl_8}$ and $\mathrm{Nb_3Br_8}$ the corresponding $\mathrm{Re}\Sigma(\omega)$ at the solutions $\omega = \varepsilon^{(\pm)}$ still have a finite slope. The fundamental gaps are thus affected by the Coulomb interaction and especially the retardation effects imprinted into $\mathrm{Re}\Sigma(\omega)$. At a first glance, the situation seems to be similar for $\mathrm{Nb_3I_8}$, but upon close inspection, we see that the gap is formed between $\omega = \varepsilon^{(\pm)}$ where the self-energies are nearly constant and similar to their static values $\mathrm{Re}\Sigma(\omega = 0) \approx [U^2/(\mp 12\tilde{t}_\perp)]$ (for the bonding and antibonding orbital, respectively). For the reduced U and enhanced $\tilde{t}_\perp$ of $\mathrm{Nb_3I_8}$,

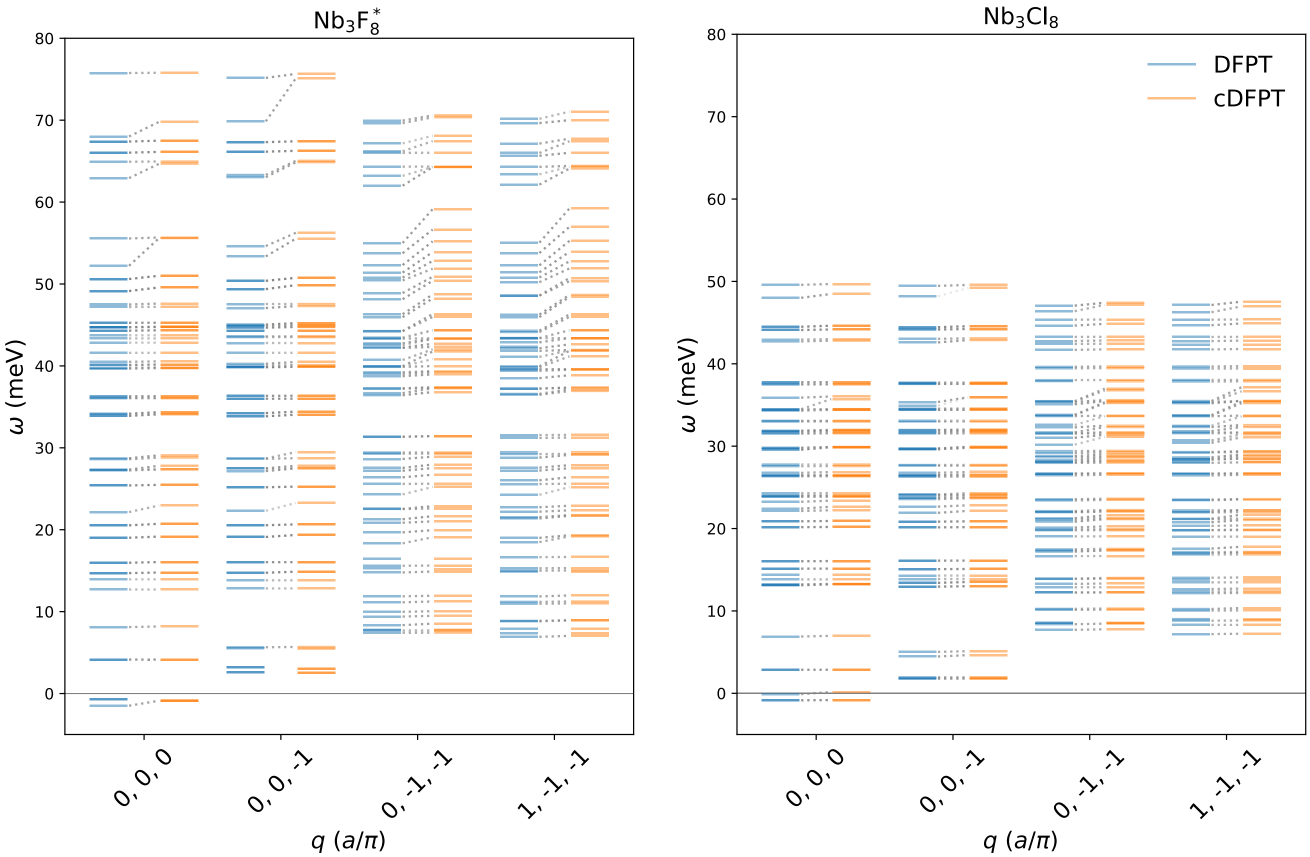

FIG. 19. Comparison between DFPT (blue/left) and cDFPT (orange/right) phonon energies of LT ($R\bar{3}m$) bulk $Nb_3F_8^*$ and Nb_3Cl_8 at selected q points. Dashed lines serve as a guide to the eye and connect DFPT with corresponding cDFPT phonon energies. No acoustic sum rules are applied.

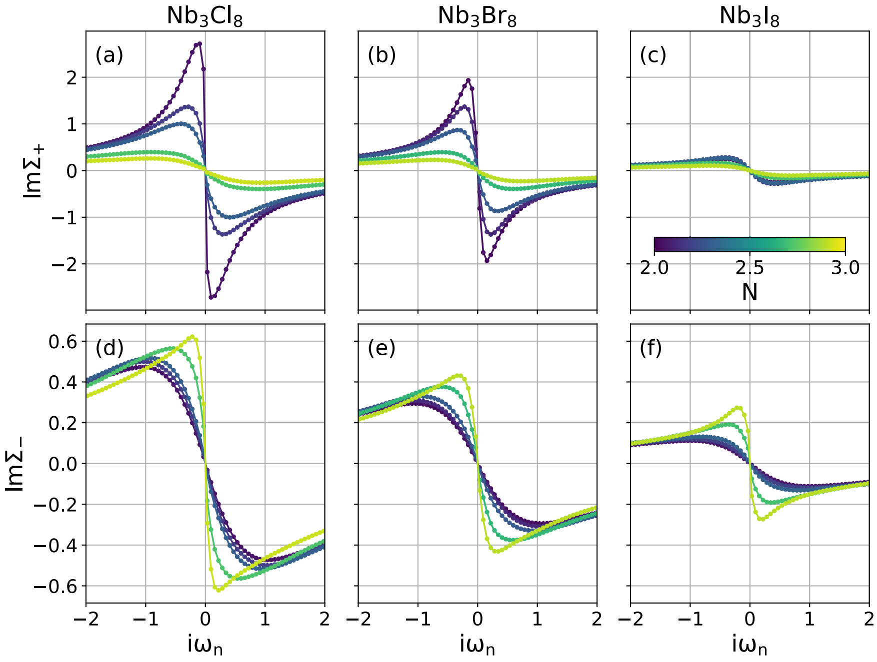

FIG. 20. Doping dependence of the imaginary Matsubara self-energy in LT ($R\bar{3}m$) bulk Nb_3X_8, for the bonding (a)–(c) and antibonding component (d)–(f).

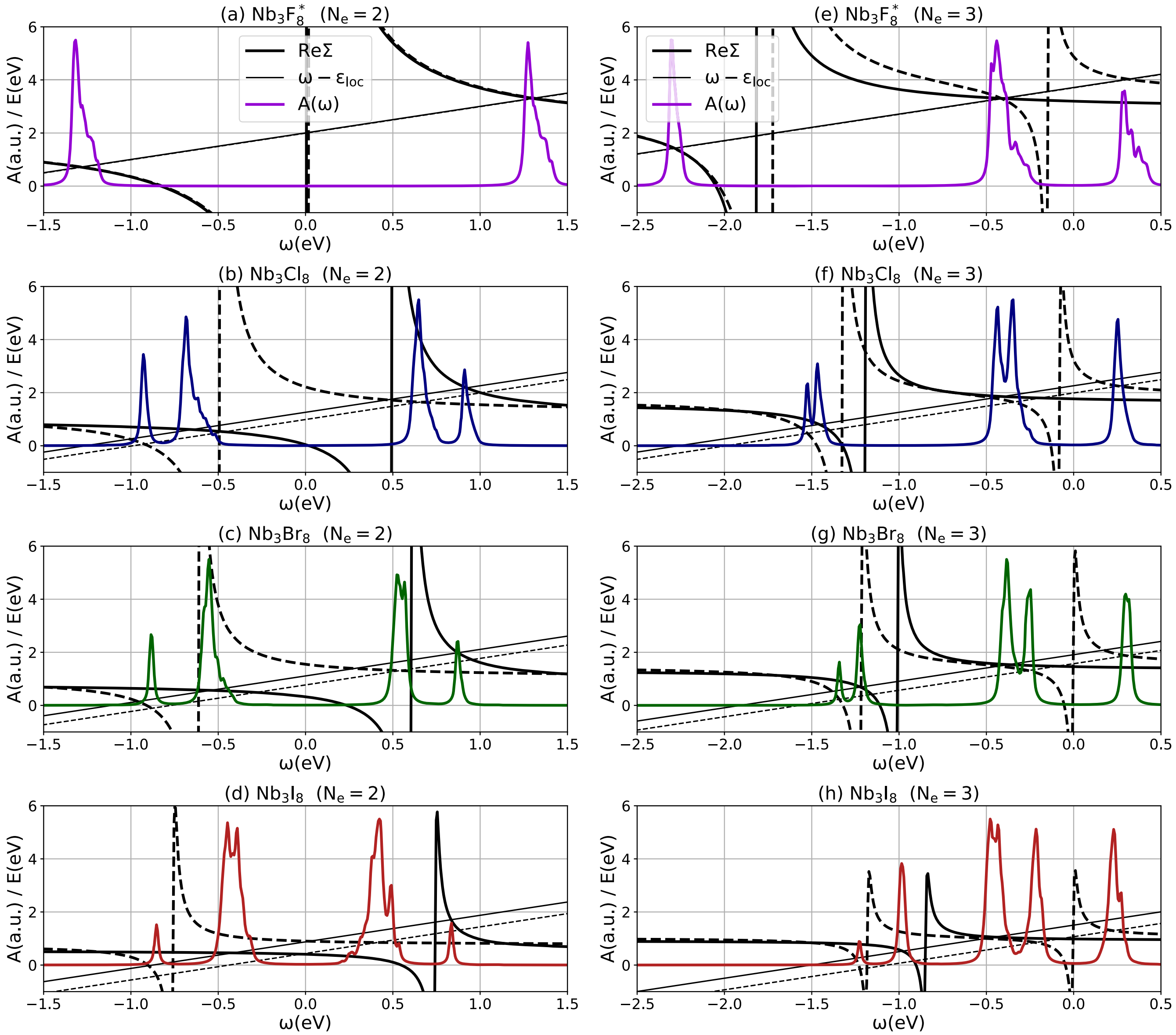

FIG. 21. Graphical representation of the local Dyson equation for the Hubbard-I calculations of LT ($R\bar{3}m$) bulk Nb_3X_8. Solid lines represent the bonding component and dashed lines represent the antibonding component. Plots in the left column (a)–(d) show the graphical solutions at half-filling (cf. Fig. 8). Plots in the right column (e)–(h) show graphical solutions at three-quarter filling: $N_e = 3$ (cf. Fig. 10).

this is dominated by $\tilde{t}_\perp$. The gap of Nb_3I_8 is thus mostly controlled by static mean-field correlations.

In the doped case with $N_e = 3$ (right column of Fig. 21) the same analysis shows that the fundamental gap between highest occupied and lowest unoccupied states is always opened due to enhanced retardation effects, but solely in the antibonding channel and in (close) vicinity of a weakly correlated state resulting from the bonding orbital (see Fig. 21 right column). This single orbital Mott-insulator behavior shows a gradual increase in gap size from Nb_3I_8 to $Nb_3F_8^*$. In the cases of $Nb_3F_8^*$ and Nb_3Cl_8 the lower Hubbard bands are so close in energy to the weakly correlated bonding band that charge transfer occurs, rendering these compounds at these doping levels correlated charge-transfer insulators.

9. Trilayer Nb_3Br_8 at half filling

In the left panel of Fig. 22 we show the Wannierized DFT band structure of a trilayer Nb_3Br_8 using the molecular orbital basis and find three rather flat bands: a half-occupied metallic one surrounded by two fully occupied or empty ones. The metallic flat band results from the weakly hybridized “surface” monolayer and the other two are the bonding or antibonding split bands from the strongly hybridized bilayer. This is in line with the discussed band structure in Ref. [31]. As argued above, this mean-field

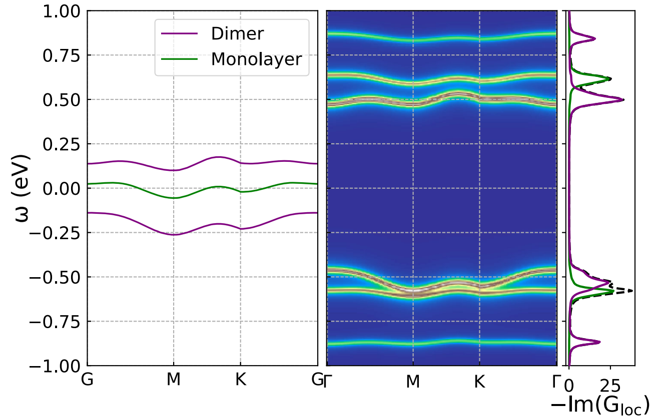

FIG. 22. Trilayer Nb_3Br_8 DFT and Hubbard-I results. Only on-site screened coulomb interaction are taken into account. U_0 is taken from the bulk cRPA calculations.

picture is not properly reflecting the strong Coulomb interaction effects in the system. Therefore, we used this single-particle band structure together with the (molecular orbital) local Coulomb interaction matrix elements as obtained from our cRPA calculations (for the bulk material) to perform cluster DMFT calculations within the Hubbard-I approximation. The result is shown in the right panel of Fig. 22. We see that the Coulomb interactions induce a gap with a set of three rather flat bands on either side of the Fermi energy. Projecting this interacting spectral function to the monolayer or bilayer basis shows that the gap is formed between bilayer states. In detail, the gap is formed, like in the bulk material, between the lower Hubbard band of the bonding orbital and the upper Hubbard band of the anti-bonding orbital. We also find a lower and upper Hubbard band of the initially metallic surface monolayer band.

The two systems (“surface monolayer” and bilayer) are almost completely separated as a result of the small hybridization between them, consistent with the interpretation of a vdW material. We expect this electronic disentanglement to be a valid pictures for all finite-stacks with unpaired surface layers. We further note that in finite-stack systems the screening to the local Coulomb interactions will be a function of the z position in the stack. The local Coulomb interaction and with it the resulting correlated gaps could thus be different in thin and thick stacks and could vary with the layer distance to the top and bottom surface.

10. Magnetic order in Nb_3X_8 monolayers and bulk

Following the effective spin-lattice Hamiltonian given by Eq. (2) in the main text, our spin dynamics simulations indicate that the ground state magnetic order for all bulk and monolayer of Nb_3X_8 exhibits conical spin spirals with in-plane propagation vector $\mathbf{q}$

$$\mathbf{S}_i^A(\mathbf{q}, \phi^A, \theta) = \begin{pmatrix} \sin(\theta)\cos(\mathbf{q}\cdot\mathbf{R}_i^A + \phi^A) \\ \sin(\theta)\sin(\mathbf{q}\cdot\mathbf{R}_i^A + \phi^A) \\ \cos(\theta) \end{pmatrix}, \tag{A5}$$

where $\mathbf{S}_i^A$ is a classical spin of sub-lattice A at site $\mathbf{R}_i^A$, θ is the cone angle, and ϕ^A the phase. In the absence of a magnetic field the spin spirals transforms from conical to flat with $\theta = \pi/2$. In such a case, inserting Eq. (A5) into the spin-lattice Hamiltonian given by Eq. (2) results in the following expression for the energy density of the exchange interaction as a function of $\mathbf{q}$ and ϕ

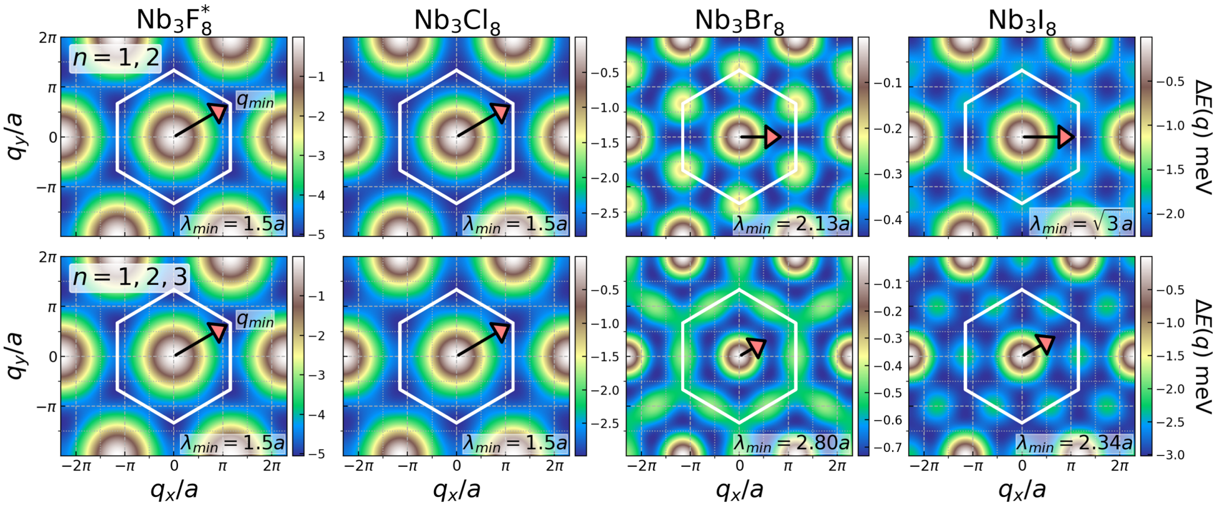

FIG. 23. Energy of the exchange interaction $\Delta E(\mathbf{q})$ as a function of the spin-spiral $\mathbf{q} = (q_x, q_y)$ vector for Nb_3X_8 monolayers. The top and bottom panels illustrate the results for exchange interactions $J_{ij}^{(n)}$ truncated to two ($n = 1, 2$) and three ($n = 1, 2, 3$) shells of nearest neighbors, respectively. The white hexagons represent the first Brillouin zone, while the arrows indicate the $\mathbf{q}_{\mathrm{min}}$ vectors corresponding to the lowest exchange interaction energy. $\lambda_{\mathrm{min}} = 2\pi/|\mathbf{q}|$ represents the period of the spin spirals and a is the in-plane lattice parameter.

TABLE V. Magnetic ground state order in bulk and monolayer Nb_3X_8 compounds. Here, $\lambda = [(2\pi)/\mathbf{q}]$ represents the period of the spin spirals, while $\Delta\phi$ is the phase difference between the spirals in the two sublattices (applicable only to bulk structures). The parameter $\alpha_{\mathbf{q}}$ specifies the direction of spin spiral propagation relative to the in-plane unit cell vector **a**, and E_{ex} denotes the corresponding energy associated with the exchange interaction (in meV).

	Bulk LT ($R\bar{3}m$) phase				Bulk HT ($P\bar{3}m1$) phase		ML			
	$Nb_3F_8^*$	Nb_3Cl_8	Nb_3Br_8	Nb_3I_8	Nb_3Cl_8	Nb_3Br_8	$Nb_3F_8^*$	Nb_3Cl_8	Nb_3Br_8	Nb_3I_8
λ	$1.5a$	$1.66a$	$3.56a$	$3.40a$	$1.72a$	$4.00a$	$1.5a$	$1.5a$	$2.8a$	$2.34a$
$\Delta\phi$	π	π	π	π	π	π				
$\alpha_{\mathbf{q}}$	0	0	0	0	0	30°	0	0	0	0
E_{ex}	−3.99	−37.61	−70.38	−185.98	−3.62	−3.94	−5.06	−3.99	−0.73	−3.02

$$E_{\mathrm{ex}}(\mathbf{q}) = -\frac{1}{2N_A}\sum_{AB}\sum_{i,j}^{N_A,N_B} J_{ij}^{AB}\cos(\mathbf{q}\cdot\mathbf{R}_{ij}^{AB} + \Delta\phi^{AB}), \tag{A6}$$

where the sum over i is restricted to the number of magnetic sites N_A in sublattice A of the magnetic unit cell and j runs over sites in sublattice B. $\mathbf{R}_{ij}^{AB} = \mathbf{R}_j^B - \mathbf{R}_i^A$ is a distance between two sites and ϕ^{AB} is a phase difference between spirals in sublatticies A and B. For all Nb_3X_8 compounds, the obtained exchange interactions J_{ij} rapidly diminish beyond the third nearest neighbors in the in-plane direction and the second nearest neighbors in the out-of-plane direction. Therefore, we truncate the sum over j to include only these neighboring distances. It is important to note that monolayers have only one sublattice and $\Delta\phi^{AB} = 0$, whereas in bulk materials there are two sublattices and $\Delta\phi^{AB}$ may assume a finite value, potentially leading to magnetic ordering in the z direction.

a. Nb_3X_8 monolayers

To determine the ground state parameters of the spin spirals in monolayers, we minimize the total energy described in Equation (A6) with respect to the wave vector **q**. Corresponding exchange interaction parameters J_{ij} are provided in Table II. Since, there is only one sublattice in monolayers, the phase ϕ is irrelevant to the results. Figure 23 illustrates the energy of the exchange interaction as a function of the wave vector **q** and the truncation distance between interacting pairs, considering up to two and three shells of nearest neighbors. The $Nb_3F_8^*$ and Nb_3Cl_8 monolayers exhibit identical propagation directions with the same value of $|\mathbf{q}_{\mathrm{min}}|$, resulting in commensurate spin spirals with a periodicity of $1.5a$ (where a is the in-plane lattice parameter), equivalent to a 120°-AFM order. While the contribution from third nearest neighbors is negligible for these two compounds, the situation changes for the Nb_3Br_8 and Nb_3I_8 monolayers. Specifically, when accounting for the third nearest neighbors in Nb_3Br_8 and Nb_3I_8, the direction of spin spiral propagation is altered, and the period of modulation increases, leading to incommensurate spin configurations. The final information about the ground state spirals and corresponding energies of the exchange interaction are summarized in Table V.

b. Nb_3X_8 bulk

Similar to the Nb_3X_8 monolayers, we investigate the magnetic properties of bulk compounds in both the low- and high-temperature phases. A notable distinction from the monolayer case is the presence of out-of-plane $J_\perp^s$ and $J_\perp^s$ exchange interactions in the bulk material, see Table III.

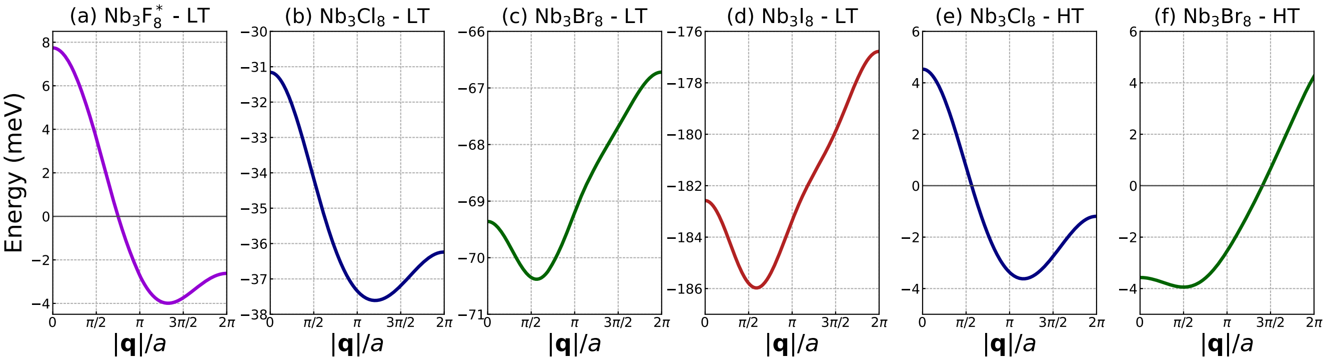

FIG. 24. Energies of the exchange interactions as a function of **q** for (a)–(d) all LT ($R\bar{3}m$) Nb_3X_8 compounds and (e)–(f) HT ($P\bar{3}m1$) Nb_3Cl_8 and Nb_3Br_8.

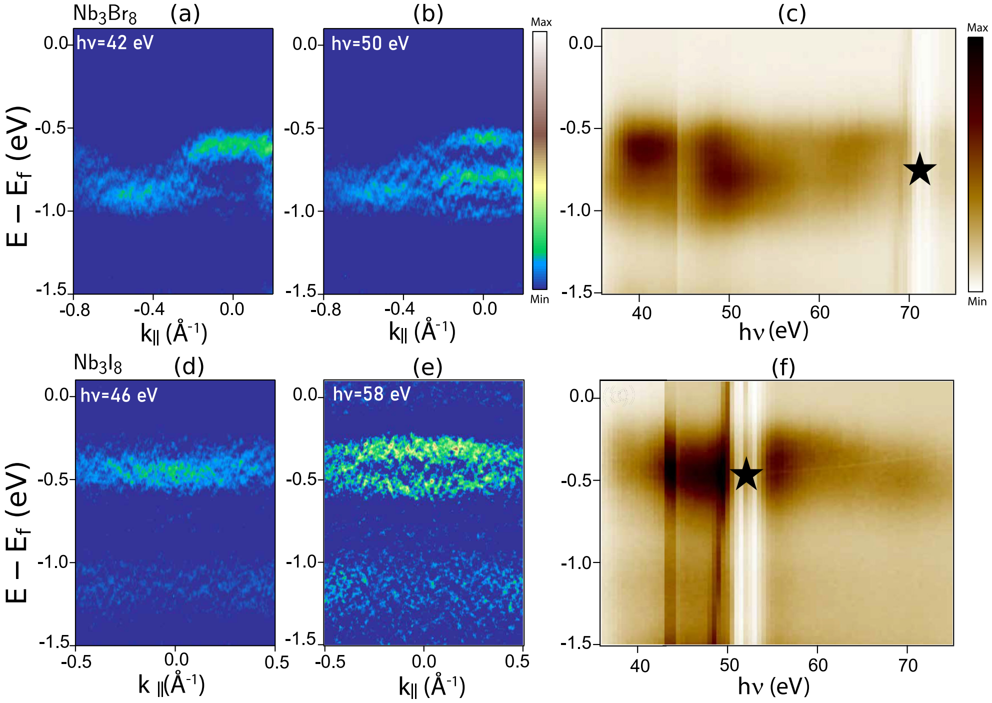

FIG. 25. (a),(b),(d),(e) 2D curvature plots. (c) and (f) The photon energy dependent ARPES data over a photon energy range of 36 to 75 eV at $k_{\parallel} = 0$.

Our spin dynamics simulations reveal that the ground state exhibits a spin spiral characterized by an in-plane propagation wave vector $\mathbf{q}$. Given this preference for in-plane propagation, we analyze the spirals in the two sublattices ($A = 1, 2$) within each layer, which are identified by a phase ϕ^{A}. To determine the ground state parameters of these spirals, we minimize the total energy described in Eq. (A6) with respect to the wave vector $\mathbf{q}$ and the phase difference ϕ^{AB}. The final results are summarized in Table V.

Figure 24 illustrates the energies of the exchange interactions as a function of q for all LT $\mathrm{Nb_3X_8}$ compounds, as well as HT $\mathrm{Nb_3Cl_8}$ and $\mathrm{Nb_3Br_8}$. The spirals associated with these energy dispersions are characterized by minimized values of $\Delta\phi$ and $\alpha_{\mathbf{q}}$, as summarized in Table V. Since $\Delta\phi = \pi$ for all cases, the magnetic order at $q = 0$ is AFM in the z-direction. From Fig. 24 it is evident that the primary contribution to the exchange energy in LT $\mathrm{Nb_3F_8^*}$ arises from in-plane spiralization. Conversely, for $\mathrm{Nb_3Br_8}$ and $\mathrm{Nb_3I_8}$, the dominant contribution comes from out-of-plane AFM order, while the energy gain from in-plane spiralization is relatively minor. In the case of $\mathrm{Nb_3Cl_8}$, although the energy contribution from in-plane spiralization is more significant, it remains less than that from the AFM order in the z direction. Turning to the HT phases, the energy gain in $\mathrm{Nb_3Cl_8}$, much like that in LT $\mathrm{Nb_3F_8^*}$, is primarily due to in-plane magnetic ordering; meanwhile, for HT $\mathrm{Nb_3Br_8}$, it arises from the out-of-plane AFM order.

11. ARPES

Figures 25(a), 25(b), 25(d), and 25(e) show the 2D curvature plots corresponding to the raw ARPES data in Figs. 8(e), 8(f), 8(g), and 8(h). Figures 25(c) and 25(f) show the raw ARPES data at $\bar{\Gamma}$ plotted against photon energy. The significant redistribution of spectral weight in energy, as visible in Figs. 25(c) and 25(f) is interpreted as the result of probing different wave vectors along the $\Gamma - A$ high-symmetry direction.

[1] G. Onida, L. Reining, and A. Rubio, *Electronic excitations: Density-functional versus many-body Green's-function approaches*, Rev. Mod. Phys. **74**, 601 (2002).

[2] A. Bostwick, F. Speck, K. Horn, M. Polini, R. Asgari, A. H. MacDonald, and E. Rotenberg, *Observation of plasmarons in quasi-freestanding doped graphene*, Science **328**, 999 (2010).

[3] F. Caruso, H. Lambert, and F. Giustino, *Band structures of plasmonic polarons*, Phys. Rev. Lett. **114**, 146404 (2015).

[4] M. Imada, A. Fujimori, and Y. Tokura, *Metal-insulator transitions*, Rev. Mod. Phys. **70**, 1039 (1998).

[5] G. Kotliar and D. Vollhardt, *Strongly correlated materials: Insights from dynamical mean-field theory*, Phys. Today **57**, No. 3, 53 (2004).

[6] D. Basov, R. Averitt, and D. Hsieh, *Towards properties on demand in quantum materials*, Nat. Mater. **16**, 1077 (2017).

[7] A. K. Geim and I. V. Grigorieva, *Van der Waals heterostructures*, Nature (London) **499**, 419 (2013).

[8] K. S. Novoselov, A. K. Geim, S. V. Morozov, D. Jiang, M. I. Katsnelson, I. V. Grigorieva, S. V. Dubonos, and A. A. Firsov, *Two-dimensional gas of massless Dirac fermions in graphene*, Nature (London) **438**, 197 (2005).

[9] J. T. Ye, Y. J. Zhang, R. Akashi, M. S. Bahramy, R. Arita, and Y. Iwasa, *Superconducting dome in a gate-tuned band insulator*, Science **338**, 1193 (2012).

[10] A. Raja, A. Chaves, J. Yu, G. Arefe, H. M. Hill, A. F. Rigosi, T. C. Berkelbach, P. Nagler, C. Schüller, T. Korn *et al.*, *Coulomb engineering of the bandgap and excitons in two-dimensional materials*, Nat. Commun. **8**, 15251 (2017).

[11] Y. Cao, V. Fatemi, A. Demir, S. Fang, S. L. Tomarken, J. Y. Luo, J. D. Sanchez-Yamagishi, K. Watanabe, T. Taniguchi, E. Kaxiras *et al.*, *Correlated insulator behavior at half-filling in magic-angle graphene superlattices*, Nature (London) **556**, 80 (2018).

[12] K. S. Burch, D. Mandrus, and J.-G. Park, *Magnetism in two-dimensional van der Waals materials*, Nature (London) **563**, 47 (2018).

[13] J. A. Wilson, F. Di Salvo, and S. Mahajan, *Charge-density waves and superlattices in the metallic layered transition metal dichalcogenides*, Adv. Phys. **24**, 117 (1975).

[14] X. Xi, Z. Wang, W. Zhao, J.-H. Park, K. T. Law, H. Berger, L. Forró, J. Shan, and K. F. Mak, *Ising pairing in superconducting* $\mathrm{NbSe_2}$ *atomic layers*, Nat. Phys. **12**, 139 (2016).

[15] Y. Cao, V. Fatemi, S. Fang, K. Watanabe, T. Taniguchi, E. Kaxiras, and P. Jarillo-Herrero, *Unconventional superconductivity in magic-angle graphene superlattices*, Nature (London) **556**, 43 (2018).

[16] L. Perfetti, A. Georges, S. Florens, S. Biermann, S. Mitrovic, H. Berger, Y. Tomm, H. Höchst, and M. Grioni, *Spectroscopic signatures of a bandwidth-controlled Mott transition at the surface of* $1T-\mathrm{TaSe_2}$, Phys. Rev. Lett. **90**, 166401 (2003).

[17] C. Butler, M. Yoshida, T. Hanaguri, and Y. Iwasa, *Mottness versus unit-cell doubling as the driver of the insulating state in* $\mathrm{1T\text{-}TaS_{22}}$, Nat. Commun. **11**, 2477 (2020).

[18] Y. Wang, H. Wu, G. T. McCandless, J. Y. Chan, and M. N. Ali, *Quantum states and intertwining phases in kagome materials*, Nat. Rev. Phys. **5**, 635 (2023).

[19] T. A. Maier, M. Jarrell, T. Pruschke, and M. Hettler, *Quantum cluster theories*, Rev. Mod. Phys. **77**, 1027 (2005).

[20] Y. Haraguchi and K. Yoshimura, *Molecular orbital electronic instability in the van der Waals kagomé semiconductor* $\mathrm{Nb_3Cl_8}$*: Exploring future directions*, J. Phys. Soc. Jpn. **93**, 111002 (2024).

[21] J. Hu, X. Zhang, C. Hu, J. Sun, X. Wang, H.-Q. Lin, and G. Li, *Correlated flat bands and quantum spin liquid state in a cluster Mott insulator*, Commun. Phys. **6**, 172 (2023).

[22] Y. Zhang, Y. Gu, H. Weng, K. Jiang, and J. Hu, *Mottness in two-dimensional van der Waals* $\mathrm{Nb_3X_8}$ *monolayers (*$X = \mathrm{Cl}$, Br*, and I)*, Phys. Rev. B **107**, 035126 (2023).

[23] S. Gao *et al.*, *Discovery of a single-band Mott insulator in a van der Waals flat-band compound*, Phys. Rev. X **13**, 041049 (2023).

[24] S. Grytsiuk, M. I. Katsnelson, E. G. C. P. van Loon, and M. Rösner, $\mathrm{Nb_3Cl_8}$*: A prototypical layered Mott-Hubbard insulator*, npj Quantum Mater. **9**, 8 (2024).

[25] M. Date *et al.*, *Momentum-resolved fingerprint of Mottness in layer-dimerized* $\mathrm{Nb_3Br_8}$, Nat. Commun. **16**, 4037 (2025).

[26] Q. Yang, M. Wu, J. Duan, Z. Ma, L. Li, Z. Huo, Z. Zhang, K. Watanabe, T. Taniguchi, X. Zhao, Y. Chen, Y. Shi, W. Jiang, K. Liu, and X. Lu, *Gate tunable room-temperature Mott insulator in kagome compound* $\mathrm{Nb_3Cl_8}$, arXiv:2506.08730.

[27] B. Liu, Y. Zhang, X. Han, J. Sun, H. Zhou, C. Li, J. Cheng, S. Yan, H. Lei, Y. Shi, H. Yang, and S. Li, *Possible quantum-spin-liquid state in van der Waals cluster magnet* $\mathrm{Nb_3Cl_8}$, J. Phys. Condens. Matter **36**, 155602 (2024).

[28] J. Mangeri, V. R. Pavizhakumari, and T. Olsen, *Magnetoelectric behavior of breathing kagomé monolayers of* $\mathrm{Nb_3(Cl,Br,I)_8}$ *from first-principles calculations*, 2D Mater. **12**, 035004 (2025).

[29] A. Carta, P. Mlkvik, F. Grahlow, M. Ströbele, H. J. Meyer, C. P. Romao, N. A. Spaldin, and C. Ederer, *Hubbard dimer physics and the magnetostructural transition in the correlated cluster material* $\mathrm{Nb_3Cl_8}$, arXiv:2509.03988.

[30] H. Wu, Y. Wang, Y. Xu, P. K. Sivakumar, C. Pasco, U. Filippozzi, S. S. Parkin, Y.-J. Zeng, T. McQueen, and M. N. Ali, *The field-free Josephson diode in a van der Waals heterostructure*, Nature (London) **604**, 653 (2022).

[31] Y. Zhang, Y. Gu, P. Li, J. Hu, and K. Jiang, *General theory of Josephson diodes*, Phys. Rev. X **12**, 041013 (2022).

[32] J. P. Sheckelton, K. W. Plumb, B. A. Trump, C. L. Broholm, and T. M. McQueen, *Rearrangement of van der Waals stacking and formation of a singlet state at* $T = 90$ K *in a cluster magnet*, Inorg. Chem. Front. **4**, 481 (2017).

[33] Y. Haraguchi, C. Michioka, M. Ishikawa, Y. Nakano, H. Yamochi, H. Ueda, and K. Yoshimura, *Magnetic–nonmagnetic phase transition with interlayer charge disproportionation of* $\mathrm{Nb_3}$ *trimers in the cluster compound* $\mathrm{Nb_3Cl_8}$, Inorg. Chem. **56**, 3483 (2017).

[34] D. A. Jeff, F. Gonzalez, K. Harrison, Y. Zhao, T. Fernando, S. Regmi, Z. Liu, H. R. Gutierrez, M. Neupane, J. Yang, J.-H. Chu, X. Xu, T. Cao, and S. I. Khondaker, *Raman study of layered breathing kagome lattice semiconductor* $\mathrm{Nb_3Cl_8}$, 2D Mater. **10**, 045030 (2023).

[35] S. Regmi, T. Fernando, Y. Zhao, A. P. Sakhya, G. Dhakal, I. Bin Elius, H. Vazquez, J. D. Denlinger, J. Yang, J.-H. Chu, X. Xu, T. Cao, and M. Neupane, *Spectroscopic evidence of flat bands in breathing kagome semiconductor* $\mathrm{Nb_33}I_8$, Commun. Mater. **3**, 100 (2022).

[36] Z. Sun, H. Zhou, C. Wang, S. Kumar, D. Geng, S. Yue, X. Han, Y. Haraguchi, K. Shimada, P. Cheng, L. Chen, Y. Shi, K. Wu, S. Meng, and B. Feng, *Observation of topological flat bands in the kagome semiconductor* $\mathrm{Nb_3Cl_8}$, Nano Lett. **22**, 4596 (2022).

[37] S. Regmi, A. P. Sakhya, T. Fernando, Y. Zhao, D. Jeff, M. Sprague, F. Gonzalez, I. Bin Elius, M. I. Mondal, N. Valadez, D. Jarrett, A. Agosto, J. Yang, J.-H. Chu, S. I. Khondaker, X. Xu, T. Cao, and M. Neupane, *Observation of flat and weakly dispersing bands in the van der Waals semiconductor* $\mathrm{Nb_3Br_8}$ *with breathing kagome lattice*, Phys. Rev. B **108**, L121404 (2023).

[38] J. Yoon, E. Lesne, K. Sklarek, J. Sheckelton, C. Pasco, S. S. P. Parkin, T. M. McQueen, and M. N. Ali, *Anomalous thickness-dependent electrical conductivity in van der*

Waals layered transition metal halide, $\mathrm{Nb_3Cl_8}$, J. Phys. Condens. Matter **32**, 304004 (2020).

[39] C. M. Pasco, I. El Baggari, E. Bianco, L. F. Kourkoutis, and T. M. McQueen, *Tunable magnetic transition to a singlet ground state in a 2D van der Waals layered trimerized kagomé magnet*, ACS Nano **13**, 9457 (2019).

[40] F. Conte, D. Ninno, and G. Cantele, *Layer-dependent electronic and magnetic properties of* $\mathrm{Nb_3I_8}$, Phys. Rev. Res. **2**, 033001 (2020).

[41] R. Peng, Y. Ma, X. Xu, Z. He, B. Huang, and Y. Dai, *Intrinsic anomalous valley Hall effect in single-layer* $\mathrm{Nb_3I_8}$, Phys. Rev. B **102**, 035412 (2020).

[42] E. A. Stepanov, *Signatures of a charge ice state in the doped Mott insulator* $\mathrm{Nb_3Cl_8}$, Phys. Rev. B **112**, 045131 (2025).

[43] J.-X. Xiong, X. Zhang, and A. Zunger, *Energy-lowering symmetry breaking creates a flat-band insulator in paramagnetic* $\mathrm{Nb_3Cl_8}$, arXiv:2408.00145.

[44] J. Kim, Y. Lee, Y. W. Choi, T. S. Jung, S. Son, J. Kim, H. J. Choi, J.-G. Park, and J. H. Kim, *Terahertz spectroscopy and DFT analysis of phonon dynamics of the layered van der Waals semiconductor* $\mathrm{Nb_3}X_8$ *(*$\mathrm{X = Cl}$*,* I*)*. ACS Omega **8**, 14190 (2023).

[45] Z. Meng, Z. Shi, H. Feng, H. Zhang, Z. Ren, Y. Du, F. Cheng, B. Ge, W. Cai, and W. Hao, *Abnormal relaxation behavior of excited electrons in the flat band of kagome compound* $\mathrm{Nb_3Cl_8}$, ACS Appl. Mater. Interfaces **16**, 57395 (2024).

[46] H. Zhou, H. Liu, H. Ji, X. Li, S. Meng, and J.-T. Sun, *Orbital degree of freedom induced multiple sets of second-order topological states in two-dimensional breathing kagome crystals*, npj Quantum Mater. **8**, 16 (2023).

[47] R. Bistritzer and A. H. MacDonald, *Moiré bands in twisted double-layer graphene*, Proc. Natl. Acad. Sci. U.S.A. **108**, 12233 (2011).

[48] W. P. Su, J. R. Schrieffer, and A. J. Heeger, *Solitons in polyacetylene*, Phys. Rev. Lett. **42**, 1698 (1979).

[49] Y. Xu, L. Elcoro, Z.-D. Song, M. G. Vergniory, C. Felser, S. S. P. Parkin, N. Regnault, J. L. Mañes, and B. A. Bernevig, *Filling-enforced obstructed atomic insulators*, Phys. Rev. B **109**, 165139 (2024).

[50] See https://www.topologicalquantumchemistry.fr/##/detail/25767 and https://www.topologicalquantumchemistry.fr/##/detail/421609.

[51] F. Aryasetiawan, M. Imada, A. Georges, G. Kotliar, S. Biermann, and A. I. Lichtenstein, *Frequency-dependent local interactions and low-energy effective models from electronic structure calculations*, Phys. Rev. B **70**, 195104 (2004).

[52] A. I. Lichtenstein and M. I. Katsnelson, *Ab initio calculations of quasiparticle band structure in correlated systems: LDA++ approach*, Phys. Rev. B **57**, 6884 (1998).

[53] G. Kotliar, S. Y. Savrasov, K. Haule, V. S. Oudovenko, O. Parcollet, and C. A. Marianetti, *Electronic structure calculations with dynamical mean-field theory*, Rev. Mod. Phys. **78**, 865 (2006).

[54] A. I. Lichtenstein and M. I. Katsnelson, *Antiferromagnetism and d-wave superconductivity in cuprates: A cluster dynamical mean-field theory*, Phys. Rev. B **62**, R9283 (2000).

[55] G. Kotliar, S. Y. Savrasov, G. Pálsson, and G. Biroli, *Cellular dynamical mean field approach to strongly correlated systems*, Phys. Rev. Lett. **87**, 186401 (2001).

[56] M. Schüler, M. Rösner, T. O. Wehling, A. I. Lichtenstein, and M. I. Katsnelson, *Optimal Hubbard models for materials with nonlocal Coulomb interactions: Graphene, silicene, and benzene*, Phys. Rev. Lett. **111**, 036601 (2013).

[57] C. Hu, H. Qu, X. Zhang, X.-Q. Wang, H.-Q. Lin, and G. Li, *Metal-insulator transition in a correlated bilayer kagome model*, Phys. Rev. B **110**, 235144 (2024).

[58] M. Bianchi, R. C. Hatch, D. Guan, T. Planke, J. Mi, B. B. Iversen, and P. Hofmann, *The electronic structure of clean and adsorbate-covered* $\mathrm{Bi_2Se_3}$*: an angle-resolved photoemission study*, Semicond. Sci. Technol. **27**, 124001 (2012).

[59] A. Wietek, R. Rossi, F. Šimkovic, M. Klett, P. Hansmann, M. Ferrero, E. M. Stoudenmire, T. Schäfer, and A. Georges, *Mott insulating states with competing orders in the triangular lattice Hubbard model*, Phys. Rev. X **11**, 041013 (2021).

[60] J. Jiang, Q. Liang, R. Meng, Q. Yang, C. Tan, X. Sun, and X. Chen, *Exploration of new ferromagnetic, semiconducting and biocompatible* $\mathrm{Nb_3}X_8$ *(*$\mathrm{X = Cl}$, Br *or I) monolayers with considerable visible and infrared light absorption*, Nanoscale **9**, 2992 (2017).

[61] B. Mortazavi, X. Zhuang, and T. Rabczuk, *A first-principles study on the physical properties of two-dimensional* Nb_3Cl_8*,* $\mathrm{Nb_3Br_8}$ *and* $\mathrm{Nb_3}I_8$, Appl. Phys. A **128**, 934 (2022).

[62] Y. Nomura and R. Arita, *Ab initio downfolding for electron-phonon-coupled systems: Constrained density-functional perturbation theory*, Phys. Rev. B **92**, 245108 (2015).

[63] J. Berges, E. G. C. P. van Loon, A. Schobert, M. Rösner, and T. O. Wehling, *Ab initio phonon self-energies and fluctuation diagnostics of phonon anomalies: Lattice instabilities from Dirac pseudospin physics in transition metal dichalcogenides*, Phys. Rev. B **101**, 155107 (2020).

[64] A. Georges, G. Kotliar, W. Krauth, and M. J. Rozenberg, *Dynamical mean-field theory of strongly correlated fermion systems and the limit of infinite dimensions*, Rev. Mod. Phys. **68**, 13 (1996).

[65] H. Zhang, Z. Shi, Z. Jiang, M. Yang, J. Zhang, Z. Meng, T. Hu, F. Liu, L. Cheng, Y. Xie, J. Zhuang, H. Feng, W. Hao, D. Shen, and Y. Du, *Topological flat bands in 2D breathing-kagome lattice* $\mathrm{Nb_3TeC_{17}}$, Adv. Mater. **35**, 2301790 (2023).

[66] J. H. Yun, M. Sung, M. Choi, K. Kim, W. Yang, D. Kim, M. J. Kim, S.-H. Her, S.-Y. Choi, T.-H. Kim, J. Y. Kim, H. W. Yeom, and J. S. Kim, *Flat-band electronic bipolarity in a Janus and kagome van der Waals semiconductor* $\mathrm{Nb_3Te_{17}}$, Adv. Mater. **37**, 2415045 (2025).

[67] L. Zhang and E. Gull, *Minimal pole representation and controlled analytic continuation of Matsubara response functions*, Phys. Rev. B **110**, 035154 (2024).

[68] L. Zhang, Y. Yu, and E. Gull, *Minimal pole representation and analytic continuation of matrix-valued correlation functions*, Phys. Rev. B **110**, 235131 (2024).

[69] S. S. Kancharla and S. Okamoto, *Band insulator to Mott insulator transition in a bilayer Hubbard model*, Phys. Rev. B **75**, 193103 (2007).

[70] H. Hafermann, M. I. Katsnelson, and A. I. Lichtenstein, *Metal-insulator transition by suppression of spin fluctuations*, Europhys. Lett. **85**, 37006 (2009).

[71] Y. Feng and Q. Yang, *Enabling triferroics coupling in breathing kagome lattice Nb3X8 ($X =$ Cl, Br, I) monolayers*, J. Mater. Chem. C **11**, 5762 (2023).

[72] S.-S. Gong, W. Zheng, M. Lee, Y.-M. Lu, and D. N. Sheng, *Chiral spin liquid with spinon fermi surfaces in the spin-1 2 triangular Heisenberg model*, Phys. Rev. B **100**, 241111 (R) (2019).

[73] K. Misaki and N. Nagaosa, *Theory of the nonreciprocal Josephson effect*, Phys. Rev. B **103**, 245302 (2021).

[74] In the monolayer limit, all four compounds host a single half-filled flat band around the Fermi level and, as a result of reduced screening, local Coulomb interaction matrix elements are larger than in the bulk (e.g., $U = 1.9$ eV for monolayer Nb_3Cl_8 [24] versus 1.5 eV in bulk according to Table I). For a surface layer in a finite stack, the expectation is that U is between the latter values, since there is screening from one side.

[75] Y. Wang, Y. Feng, J. G. Cheng, W. Wu, J. L. Luo, and T. F. Rosenbaum, *Spiral magnetic order and pressure-induced superconductivity in transition metal compounds*, Nat. Commun. **7**, 13037 (2016).

[76] A. Pergament, *Metal–insulator transition: The Mott criterion and coherence length*, J. Phys. Condens. Matter **15**, 3217 (2003).

[77] A. Kokin, *Metal-dielectric phase transition in an electric field*, Fiz. Tverd. Tela **17**, 1317 (1975).

[78] A. Kokin, *Low-frequency current fluctuations in systems with a semi-conductor to metal phase transformation*, Fiz. Tverd. Tela **18**, 3384 (1976).

[79] S. Nikolaev, I. Solovyev, and S. Streltsov, *Quantum spin liquid and cluster Mott insulator phases in the* Mo_3O_8 *magnets*, npj Quantum Mater. **6**, 25 (2021).

[80] J. P. Pouget, H. Launois, T. M. Rice, P. Dernier, A. Gossard, G. Villeneuve, and P. Hagenmuller, *Dimerization of a linear Heisenberg chain in the insulating phases of* $V_{1-x}Cr_xO_2$, Phys. Rev. B **10**, 1801 (1974).

[81] S. Biermann, A. Poteryaev, A. I. Lichtenstein, and A. Georges, *Dynamical singlets and correlation-assisted Peierls transition in* VO_2, Phys. Rev. Lett. **94**, 026404 (2005).

[82] M. W. Haverkort, Z. Hu, A. Tanaka, W. Reichelt, S. V. Streltsov, M. A. Korotin, V. I. Anisimov, H. H. Hsieh, H.-J. Lin, C. T. Chen, D. I. Khomskii, and L. H. Tjeng, *Orbital-assisted metal-insulator transition in* VO_2, Phys. Rev. Lett. **95**, 196404 (2005).

[83] T. C. Koethe, Z. Hu, M. W. Haverkort, C. Schüßler-Langeheine, F. Venturini, N. B. Brookes, O. Tjernberg, W. Reichelt, H. H. Hsieh, H.-J. Lin, C. T. Chen, and L. H. Tjeng, *Transfer of spectral weight and symmetry across the metal-insulator transition in* VO_2, Phys. Rev. Lett. **97**, 116402 (2006).

[84] J. M. Tomczak and S. Biermann, *Effective band structure of correlated materials: The case of* VO_2, J. Phys. Condens. Matter **19**, 365206 (2007).

[85] J. M. Tomczak, F. Aryasetiawan, and S. Biermann, *Effective band structure in the insulating phase versus strong dynamical correlations in metallic* VO_2, Phys. Rev. B **78**, 115103 (2008).

[86] J. B. Goodenough, *The two components of the crystallographic transition in* VO_2, J. Solid State Chem. **3**, 490 (1971).

[87] A. Zylbersztejn and N. F. Mott, *Metal-insulator transition in vanadium dioxide*, Phys. Rev. B **11**, 4383 (1975).

[88] J. Aretz, S. Grytsiuk, H. U. R. Strand, E. G. C. P. van Loon, and M. Rösner, Nb_3X_8 *Model Database* (2025), https://github.com/malte-roesner/Nb3X8.

[89] N. Bittner, D. Golež, M. Eckstein, and P. Werner, *Photoenhanced excitonic correlations in a Mott insulator with nonlocal interactions*, Phys. Rev. B **101**, 085127 (2020).

[90] E. G. C. P. van Loon, M. Schüler, D. Springer, G. Sangiovanni, J. M. Tomczak, and T. O. Wehling, *Coulomb engineering of two-dimensional Mott materials*, npj 2D Mater. Appl. **7**, 47 (2023).

[91] P.-O. Downey, O. Gingras, C.-D. Hébert, M. Charlebois, and A.-M. S. Tremblay, *Doping the Mott insulating state of the triangular-lattice Hubbard model reveals the Sordi transition*, Phys. Rev. B **110**, L121109 (2024).

[92] I. Silber, S. Mathimalar, I. Mangel, A. K. Nayak, O. Green, N. Avraham, H. Beidenkopf, I. Feldman, A. Kanigel, A. Klein, M. Goldstein, A. Banerjee, E. Sela, and Y. Dagan, *Two-component nematic superconductivity in* 4Hb-TaS_2, Nat. Commun. **15**, 824 (2024).

[93] L. Crippa, H. Bae, P. Wunderlich, I. I. Mazin, B. Yan, G. Sangiovanni, T. Wehling, and R. Valentí, *Heavy fermions vs doped Mott physics in heterogeneous Ta-dichalcogenide bilayers*, Nat. Commun. **15**, 1357 (2024).

[94] G. Mazza, A. Amaricci, and M. Capone, *Interface and bulk superconductivity in superconducting heterostructures with enhanced critical temperatures*, Phys. Rev. B **103**, 094514 (2021).

[95] J. P. Perdew, K. Burke, and M. Ernzerhof, *Generalized gradient approximation made simple*, Phys. Rev. Lett. **77**, 3865 (1996).

[96] P. E. Blöchl, *Projector augmented-wave method*, Phys. Rev. B **50**, 17953 (1994).

[97] G. Kresse and J. Furthmüller, *Efficient iterative schemes for ab initio total-energy calculations using a plane-wave basis set*, Phys. Rev. B **54**, 11169 (1996).

[98] G. Kresse and D. Joubert, *From ultrasoft pseudopotentials to the projector augmented-wave method*, Phys. Rev. B **59**, 1758 (1999).

[99] A. A. Mostofi, J. R. Yates, Y.-S. Lee, I. Souza, D. Vanderbilt, and N. Marzari, *WANNIER90: A tool for obtaining maximally-localised Wannier functions*, Comput. Phys. Commun. **178**, 685 (2008).

[100] M. Kaltak, *Merging GW with DMFT*, Ph.D. thesis, University of Vienna, 2015.

[101] O. Parcollet, M. Ferrero, T. Ayral, H. Hafermann, I. Krivenko, L. Messio, and P. Seth, *TRIQS: A toolbox for research on interacting quantum systems*, Comput. Phys. Commun. **196**, 398 (2015).

[102] M. Schüler, *TRIQS/HubbardI—a Hubbard-I solver based on triqs atom_diag* (2022).

[103] P. Werner, A. Comanac, L. de' Medici, M. Troyer, and A. J. Millis, *Continuous-time solver for quantum impurity models*, Phys. Rev. Lett. **97**, 076405 (2006).

[104] P. Werner and A. J. Millis, *Hybridization expansion impurity solver: General formulation and application to Kondo lattice and two-orbital models*, Phys. Rev. B **74**, 155107 (2006).

[105] K. Haule, *Quantum Monte Carlo impurity solver for cluster dynamical mean-field theory and electronic structure calculations with adjustable cluster base*, Phys. Rev. B **75**, 155113 (2007).

[106] E. Gull, A. J. Millis, A. I. Lichtenstein, A. N. Rubtsov, M. Troyer, and P. Werner, *Continuous-time Monte Carlo methods for quantum impurity models*, Rev. Mod. Phys. **83**, 349 (2011).

[107] M. Wallerberger, A. Hausoel, P. Gunacker, A. Kowalski, N. Parragh, F. Goth, K. Held, and G. Sangiovanni, *w2dynamics: Local one- and two-particle quantities from dynamical mean field theory*, Comput. Phys. Commun. **235**, 388 (2019).

[108] P. Gunacker, M. Wallerberger, E. Gull, A. Hausoel, G. Sangiovanni, and K. Held, *Continuous-time quantum Monte Carlo using worm sampling*, Phys. Rev. B **92**, 155102 (2015).

[109] P. Gunacker, M. Wallerberger, T. Ribic, A. Hausoel, G. Sangiovanni, and K. Held, *Worm-improved estimators in continuous-time quantum Monte Carlo*, Phys. Rev. B **94**, 125153 (2016).

[110] J. Kaye, K. Chen, and O. Parcollet, *Discrete Lehmann representation of imaginary time Green's functions*, Phys. Rev. B **105**, 235115 (2022).

[111] J. Kaye, K. Chen, and H. U. R. Strand, *libdlr: Efficient imaginary time calculations using the discrete Lehmann representation*, Comput. Phys. Commun. **280**, 108458 (2022).

[112] J. Kaye, H. U. R. Strand, and N. Wentzell, *cppdlr: Imaginary time calculations using the discrete Lehmann representation*, J. Open Source Software **9**, 6297 (2024).

[113] L.-F. Arsenault, P. Sémon, and A.-M. S. Tremblay, *Benchmark of a modified iterated perturbation theory approach on the fcc lattice at strong coupling*, Phys. Rev. B **86**, 085133 (2012).

[114] P. Giannozzi *et al.*, *QUANTUM ESPRESSO: A modular and open-source software project for quantum simulations of materials*, J. Phys. Condens. Matter **21**, 395502 (2009).

[115] P. Giannozzi *et al.*, *Advanced capabilities for materials modelling with quantum espresso*, J. Phys. Condens. Matter **29**, 465901 (2017).

[116] M. Schlipf and F. Gygi, *Optimization algorithm for the generation of ONCV pseudopotentials*, Comput. Phys. Commun. **196**, 36 (2015).

[117] J. Berges, A. Schobert, E. G. C. P. van Loon, M. Rösner, and T. O. Wehling, *elphmod: PYTHON modules for electron-phonon models*, 10.5281/zenodo.5919991.

[118] H.-K. Tang, I. Yudhistira, U. Chattopadhyay, M. Ulybyshev, P. Sengupta, F. F. Assaad, and S. Adam, *Spectral functions of lattice fermions on the honeycomb lattice with Hubbard and long-range Coulomb interactions*, Phys. Rev. B **110**, 155120 (2024).

[119] G. P. Müller, M. Hoffmann, C. Dißelkamp, D. Schürhoff, S. Mavros, M. Sallermann, N. S. Kiselev, H. Jónsson, and S. Blügel, *Spirit: Multifunctional framework for atomistic spin simulations*, Phys. Rev. B **99**, 224414 (2019).

[120] S. Hoffmann, C. Søndergaard, C. Schultz, Z. Li, and P. Hofmann, *An undulator-based spherical grating monochromator beamline for angle-resolved photoemission spectroscopy*, Nucl. Instrum. Methods Phys. Res., Sect. A **523**, 441 (2004).

[121] M. Rösner, E. Şaşıoğlu, C. Friedrich, S. Blügel, and T. O. Wehling, *Wannier function approach to realistic Coulomb interactions in layered materials and heterostructures*, Phys. Rev. B **92**, 085102 (2015).

[122] J. M. Tomczak, *Propriétés spectrales et optiques des Matériaux corrélés*, Thesis, Ecole Polytechnique X, 2007.

[123] E. G. C. P. van Loon, J. Berges, and T. O. Wehling, *Downfolding approaches to electron-ion coupling: Constrained density-functional perturbation theory for molecules*, Phys. Rev. B **103**, 205103 (2021).